AGU PUBLICATIONS

JGR

Journal of Geophysical Research: Space Physics

RESEARCH ARTICLE
10.1002/2017JA023988

Key Points:
- We introduce a new method that estimates both the number of unknown traveling ionospheric disturbances and its parameters from GNSS data
- The method has been successfully assessed with simulated data (on real pierce point locations) and real data from GEONET in Japan
- This new approach can be applied to other regions with dense GNSS networks and can be extended to study seismic-related ionospheric waves

Correspondence to:
H. Yang,
h.yang@upc.edu

Citation:
Yang, H., E. Monte-Moreno, and M. Hernández-Pajares (2017), Multi-TID detection and characterization in a dense Global Navigation Satellite System receiver network, *J. Geophys. Res. Space Physics*, *122*, 9554–9575, doi:10.1002/2017JA023988.

Received 3 FEB 2017
Accepted 26 JUL 2017
Accepted article online 31 JUL 2017
Published online 5 SEP 2017

©2017. American Geophysical Union. All Rights Reserved.

Multi-TID detection and characterization in a dense Global Navigation Satellite System receiver network

Heng Yang[1], **Enrique Monte-Moreno**[1], **and Manuel Hernández-Pajares**[2]

[1]Department of Signal Theory and Communications, TALP, Universitat Politècnica de Catalunya, Barcelona, Spain, [2]Department of Applied Mathematics IV, IonSAT, Universitat Politècnica de Catalunya, Barcelona, Spain

Abstract The medium-scale traveling ionospheric disturbances (MSTIDs) constitute the most frequent ionospheric wave signatures. We propose a method for detecting the number of simultaneous MSTIDs from a time series of high-pass-filtered Vertical Total Electron Content (VTEC) maps and their parameters. The method is tested on the VTEC map corresponding to a simulated realistic scenario and on actual data from dual-frequency Global Positioning System (GPS) measurements gathered by +1200 GPS receivers of the GPS Earth Observation Network (GEONET) in Japan. The contribution consists of the detection of the number of independent MSTIDs from a nonuniform sampling of the ionospheric pierce points. The problem is set as a sparse decomposition on elements of a dictionary of atoms that span a linear space of possible MSTIDs. These atoms consist of plane waves characterized by a wavelength, direction, and phase on a surface defined, the part of the ionosphere sounded by the GEONET (i.e., 25°N to 50°N of latitude and 125°E to 155°E of longitude). The technique is related to the atomic decomposition and least absolute shrinkage and selection operator. The geophysical contribution of this paper is showing (a) the detection of several simultaneous MSTIDs of different characteristics, with a continuous change in the velocity; (b) detection of circular MSTID waves compatible by time and center with a specific earthquake; (c) simultaneous superposition of two distinct MSTIDs, with almost the same azimuth; and (d) the presence at nighttime of MSTIDs with velocities in the range 400–600 m/s.

1. Introduction

The ionosphere is the region of the Earth's atmosphere defined by its free electron population and located between approximately 50 to 1000 km altitude. The most frequent wave-like structures of the electron density are called medium-scale traveling ionospheric disturbances (MSTIDs), presenting variations up to a few total electron content units (TECUs) of amplitudes in solar cycle maximum conditions (1 TECU = 10^{16} el/m^2 which correspond to a ≈16 cm delay in L1 GPS signal). The MSTIDs have different properties in relation to the temporal and spatial variation. Typically, the MSTIDs occurring in midlatitude are roughly characterized by periods between 15 and 60 min, horizontal wavelengths between 50 and 300 km, and velocities between 100 and 300 m/s, with propagation toward the equator at daytime in local fall and winter seasons and toward the west at night in local spring and summer seasons [see *Hunsucker*, 1982; *Hernández-Pajares et al.*, 2006]. Their origins include the response to atmospheric gravity waves [*Hocke and Schlegel*, 1996], the Solar Terminator [*Hernández-Pajares et al.*, 2006], the Perkins instability [*Kelley*, 2011], the interhemispheric coupling effect [*Otsuka et al.*, 2004], and others. Although the MSTID perturbation may be small compared to background electron densities, significant effects are observed in electromagnetic waves propagating through the affected ionospheric region. In particular, the Global Navigation Satellite System (GNSS) signals, like the Global Positioning System (GPS) signals, are affected by the time-varying and space-varying delays of the electron fluctuation densities associated with the MSTIDs. This effect can be exploited to use the GNSS system as a global ionospheric sensor (or "ionoscope") for detecting and characterizing the MSTIDs [see *Hernández-Pajares et al.*, 2012]. The use of the GNSS for studying the ionosphere has the benefit of using a large-scale, preexisting observation network, which contrasts with other techniques that are more specific and local, such as the Low-Frequency Array [*Mevius et al.*, 2016], OI 630.0 nm all-sky images [*Stefanello et al.*, 2015] and AM radio transmissions [*Chilcote et al.*, 2015].

Prior GNSS MSTID studies include *Hunsucker* [1982], *Hocke and Schlegel* [1996], and *Hernández-Pajares et al.* [2006], which use a horizontal planar wave model over a fixed-height ionospheric thin shell around the earth. Also, *Lee et al.* [2008], *Ssessanga et al.* [2015], and *Chen et al.* [2016] estimate a three-dimensional (3-D) structure of electron density for modeling the MSTID at variable heights by means of computerized ionospheric tomography from the large dense GNSS network. Using as source data a GNSS network, *Saito et al.* [1998] and *Tsugawa et al.* [2006, 2007a, 2007b] show a high-resolution 2-D mapping of the typical daytime and nighttime MSTID waves with their properties. The above mentioned 2-D mappings have been validated by other observational techniques, for instance, the OI 630.0 nm all-sky imagers [*Shiokawa et al.*, 2003] and the Super Dual Auroral Radar Network HF radars [*Ogawa et al.*, 2009]. An additional method is proposed in *Ding et al.* [2011] and *Huang et al.* [2016], where they use a cross-spectra method to obtain the MSTID parameters from the GPS TEC series. An alternative is *Deng et al.* [2013] where the parameters of a unique MSTID plane wave are computed by spectrum analysis techniques from one-dimensional (1-D) space of detrended VTEC profiles from the 2-D maps.

Another method for characterizing the MSTIDs using GNSS was proposed in *Hernández-Pajares et al.* [2006, 2012, 2017] where the authors introduce the comprehensive GNSS ionospheric interferometry (cGII) method that estimates the characteristics of the MSTIDs, assuming a unique planar wave from the received signal of several neighboring GNSS receivers. This method computes the instantaneous wave parameters (i.e., velocity, azimuth, and wavelength) at every epoch, at the line-of-sight paths through the ionosphere from moving satellites to permanent receivers. One limitation in common with the previous methods is that this method only estimates the parameters of the dominant MSTID wave. In addition to the detection of the dominant MSTID, in this paper, we are interested in detecting and characterizing multiple simultaneous MSTIDs, which might have different origins and parameters.

In this work, we propose a multiwave parameter estimation model for detecting simultaneously the number of MSTIDs present and corresponding parameters of each disturbance. This method, which we refer to as the Atomic Decomposition Detector of MSTIDs (ADDTID), comprises the following:

1. The construction of a time series of detrended VTEC maps. This is done from observational data of dense and nonuniform distributed receivers of the GNSS network, such as the GPS Earth Observation Network (GEONET) in Japan or the California GPS Network in America.
2. The method also comprises the construction of a redundant dictionary, i.e., a set of elements that span the space of possible MSTID waves traveling on the VTEC maps. The cardinality of the dictionary will be much higher than the dimensionality of the space and will be used to reconstruct the observed detrended VTEC maps. The elements of the dictionary will consist of snapshots of planar waves at a realistic range of parameters.
3. The method performs a sparse reconstruction of the observed detrended VTEC map from a small subset of elements of the redundant dictionary. This is done by solving an optimization problem based on the norms ℓ_1 and ℓ_2. The number of selected elements of the dictionary will give the estimated number of MSTIDs present and the properties of each MSTID, i.e., amplitude, propagation azimuth, wavelength, and velocity. The technique for the sparse reconstruction is based on ideas of atomic decomposition [*Chen et al.*, 2001] and the Least Absolute Shrinkage and Selection Operator (LASSO) [*Tibshirani*, 1996].

2. Description of the Experimental Data

To test the Atomic Decomposition Detector of MSTIDs (ADDTID) method, we will use data from a dense network of receivers for constructing a time series of detrended VTEC maps. The data come from the GPS Earth Observation Network (GEONET), which consists of over 1200 GPS stations densely distributed in Japan (see Figure 1, left) [*Sagiya*, 2004].

2.1. Generation of the VTEC Maps From the GNSS Measurements

The ionospheric combination (also called geometry-free combination) L_I is computed from the carrier phase difference between L_1 and L_2 in length units, which is an affine function of the slant total electron content (STEC), i.e., the integrated electron density of the line-of-sight path in the ionosphere from the satellite j to the ith receiver, at each sample epoch t [see *Hernández-Pajares et al.*, 2002], given as

$$L_{I_i}^j(t) = {L_1}_i^j(t) - {L_2}_i^j(t) = \alpha S_i^j(t) + B_{I_i}^j(t) + w_i^j(t) \quad (1)$$

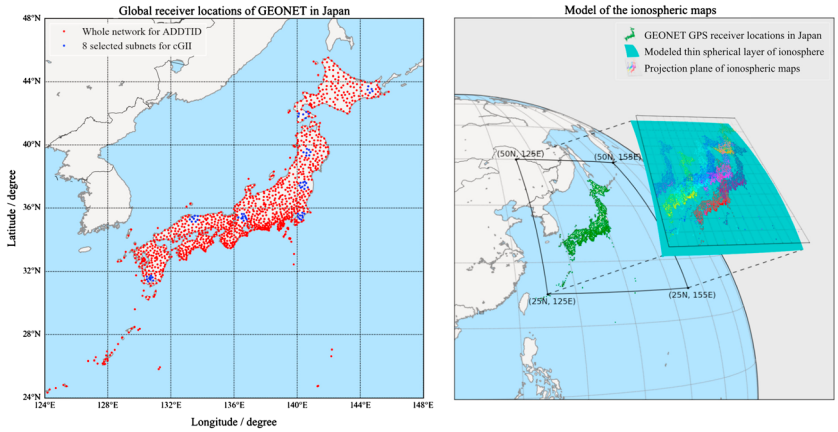

Figure 1. (left) Distribution of GPS receivers in the Japan GEONET network and (right) IPPs distribution in the ionospheric map for different satellites.

where the linear coefficient α has the approximate value $\alpha \approx 0.105$ m/TECU and the wind-up term $w_i^j(t)$, originating from the relative rotation between the satellite and receiver antennas, is typically at centimeter level and supposed to be corrected. $B_{l_i}^j(t)$, is the time-variable bias, encompassing the carrier phase ambiguities (the unknown integer number of carrier wavelengths and the noninteger satellite and receiver-dependent terms) due to receiver losses of lock, i.e., cycle slips. The bias $B_{l_i}^j(t)$ remains almost constant when no new losses of lock occur, so we split $L_{l_i}^j(t)$ into independent subseries defined by the cycle slips. $S_i^j(t)$ represents trends such as diurnal variations and elevation angle variation, which are characterized by extremely low frequencies and very high energies. This contrasts typical MSTID waveform characteristics, which consist of higher-frequency components with lower energies. The separation of the component related to the MSTID, from other components, is done by a double difference of the time series (i.e., band-pass filter) of measured $L_{l_i}^j(t)$, which we will denote as $\tilde{S}_i^j(t)$ [see *Hernández-Pajares et al.*, 2006]. In the intervals between cycle slips, the term $B_{l_i}^j$ can be considered constant and thus can be eliminated by the double time difference,

$$\tilde{S}_i^j(t) \approx L_{l_i}^j(t) - \frac{1}{2}\left[L_{l_i}^j(t+\Delta t) + L_{l_i}^j(t-\Delta t)\right] \tag{2}$$

where Δt is the detrending time interval, set to 300 s, and enhances the frequency band of the MSTIDs. When the corresponding line-of-sight path in the ionosphere is long enough, we can compute VTEC from the STEC by means of a mapping function $M(t)$ approximation, assuming that a thin spherical layer is placed at a mean effective height [see *Hernández-Pajares et al.*, 2009]. Also, we discarded observations with an elevation angle of less than 30° to reduce the effect of any mapping function error. We define the detrended and projected VTEC, $\tilde{V}_i^j(t)$, as the projection of the $\tilde{S}_i^j(t)$ by means of the mapping function $M(t)$ [see *Hernández-Pajares et al.*, 2011], that is, $\tilde{V}_i^j(t) = \frac{\tilde{S}_i^j(t)}{M(t)}$.

2.2. Model of the Ionospheric Maps

In our model, the detrended VTEC $\tilde{V}_i^j(t)$ (satellite j and station i) contains the MSTIDs signal at the ionospheric pierce points (IPPs) located on a shell with the mean effective height where we assume that the MSTID occurs. In contrast with the global ionospheric maps (GIMs) of VTEC on a worldwide scale [*Dow et al.*, 2009], we reconstruct the ionospheric activity maps at a smaller scale, with a higher resolution of space-time, and generate a localized time series of snapshots of the maps (for a similar precedent, see *Tsugawa et al.* [2007a, 2007b]).

We will denote the set of observed detrended VTECs $\tilde{V}_i^m(t)$ as $\tilde{V}_i^m(\phi, \lambda, t)$ (see equation (3)), i.e., a function of IPP geocentric latitude ϕ, longitude λ, and sample epoch t. The construction of this variable is as follows: for each satellite m and for each station i, we create a list of measurement $\tilde{V}_i^m(\phi, \lambda, t)$ at the IPP. Only satellites with elevations of >30° are used. Another selection filter includes only MSTID activity maps with more than 1000 IPPs (i.e., with more than 80% of the potential measurements available). Thus,

$$\tilde{V}^m(\phi, \lambda, t) = \left[\tilde{V}_1^m(\phi, \lambda, t), .., \tilde{V}_i^m(\phi, \lambda, t), .., \tilde{V}_N^m(\phi, \lambda, t)\right] \tag{3}$$

In Figure 1 (right), we show the detrended VTEC $\{\tilde{V}^m(\phi, \lambda, t), m = 1, 2, \ldots, M\}$ for all the observable satellites. Note that the set of IPPs due to each satellite will be different and is the source of the difficulty of the estimation problem. This is because the estimation must be performed from a nonuniform 2-D distribution of the observations, with variable spatial density. In addition, the different elevations of the satellites will give a different signal-to-noise ratio.

The range of the measured detrended VTEC by each satellite is different; thus, to improve the estimation process, the map $\tilde{V}^m(\phi, \lambda, t)$ of each satellite was normalized, assigning the value 1.0 to the 95% quantile and 0.0 to the 5% quantile. The upper and lower trimming was done so as not to bias the scale because of the outliers. Each satellite is scaled independently of the other. To not clutter the notation, henceforth, the MSTID activity map $\tilde{V}^m(\phi, \lambda, t)$ at epoch t of satellite m will be denoted as $\tilde{V}(\phi, \lambda)$.

The variable $\tilde{V}(\phi, \lambda)$ is a 2-D map, of the local time variation of the detrended VTEC. This map can be expressed in more convenient coordinates as $\tilde{V}(x, y)$ by the transformation of the pierce points from latitude-longitude-height coordinates (ϕ, λ, h) to east-north-up coordinates (x, y, z). These east-north-up coordinates (x, y, z) are projected to the plane, i.e., horizontal coordinates (x, y). The approximation of the spherical section by a plane introduces a negligible error which is minimized by assuming the center of mass of the pierce points set as the reference point of east-north-up coordinates. The map size is set from 25°N to 50°N of latitude and 125°E to 155°E of longitude, which covers GEONET. The distortion gives an error on sizes of less than 0.16%.

From Figure 1 (right), at a given epoch t, the image consists of a nonuniform 2-D sampled representation of the IPPs at the effective height, which we will model as a linear combination of Kronecker deltas located at the set of pierce points coordinates,

$$\tilde{V}(x, y) = \sum_{(x_i, y_j) \in I_{x,y}} \alpha_{i,j} \delta\left(x - x_i, y - y_j\right) \tag{4}$$

where $I_{x,y}$ is the set of coordinates (x_i, y_j) of the IPP, i.e., the coordinates of effective height (i.e., at the average MSTID activity height) of the line of sight that joins the base station and the satellite, and $\alpha_{i,j}$ is proportional to the detrended VTEC at the coordinates (x_i, y_j) in the set $I_{x,y}$. The sampling is not uniform, as the samples are originated by the pierce points of the satellites, and each satellite is associated with a set of points that mimics the shape of the projection of the stations to the effective height, as can be seen in Figure 1 (right). Another effect is that the SNR depends on the elevation of the satellite line of sight with respect to the receivers. The satellites are selected by an elevation mask of 30°.

3. Justification of the Planar Wave Model

The problem to be solved consists of detecting and characterizing an unknown set of simultaneous MSTIDs and their properties, from a detrended VTEC map with nonuniform sampling, and spatially varying SNR. In addition to an irregular and nonuniform spatial sampling, the model should deal with the directional bias associated with the geographical distribution of the stations. This directional bias is because the samples are aligned in directions that follow the underlying geography of the Japanese network (SW to NE). The model MSTID should consider the following:

1. The fact that by visual inspection, the underlying structure of the MSTID signal sometimes appears as a superposition of several plane waves [see *Hernández-Pajares et al.*, 2006]. Figures 2a–2d show the interference pattern due to several waves of similar amplitude.
2. The complexity of the estimation process. As shown in Appendix A1, each additional parameter of the model entails an increase in the size of the optimization problem, which is proportional to the product of the number of possible values of the parameters that define the atoms of the dictionary. Therefore, we have limited the model to plane waves. The inclusion of the terms that allow for modeling circular waves (this will be considered in future research) would make the problem more difficult from the computational point of view.
3. The GEONET set of receivers is located in a region that is elongated, which introduces a bias in the estimation of the parameters of the waves. For instance, in Figures 2e–2h, the number of cycles observed for a given wave depends on the azimuth.

In this paper, we will limit our model to the estimation of superposition of planar waves.

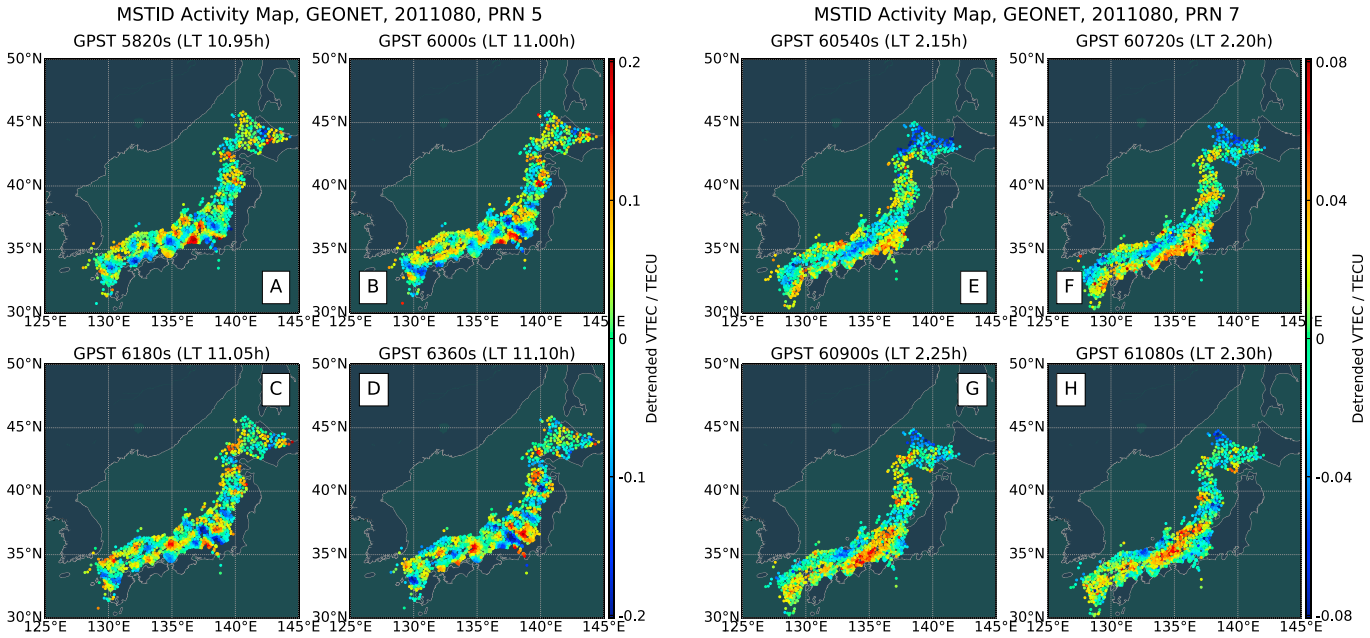

Figure 2. Wavefront propagation directly seen in the detrended VTEC maps (in TECUs) that illustrate daytime and nighttime MSTIDs, from GEONET, on the 80th day of 2011. (a–d) The detrended VTEC maps near local noon (10:57–11:06 LT) for satellite PRN 5 (four sampling GPS time epochs 5820, 6000, 6180, and 6360 s). (e–h) The detrended VTEC maps near local midnight (2:09–2:18 LT) for satellite PRN 7 (four sampling GPS time epochs 60540, 60720, 60900, and 61080 s).

4. Justification of the Estimation Method

Before developing the ADDTID method, we attempted to solve the problem of nonuniform sampling by transforming the maps into regular grids of points on which the estimation of the MSTIDs was conducted. The following techniques were attempted: interpolation by means of 2-D low-pass filtering, the Fourier transform of the smoothed 2-D sampled data, the Hough transformation, and kriging. All of which gave unsatisfactory results.

The approach that we propose is based on both the atomic decomposition of signals [*Chen et al.*, 2001] and the LASSO [*Tibshirani*, 1996], which allows for extracting a sparse signal representation from highly overcomplete dictionaries. Each atom of the dictionary represents a possible MSTID. Note that although both of the approaches are equivalent, the former emphasizes the structure of the dictionary, while the later the estimation aspects of the problem.

The approach consists of the decomposition of a signal in the span over an overdetermined dictionary and introducing a penalty in the norm of the weights of the span to obtain a sparse solution. The formal specification of the method is described in detail in section 5.2. The loss function consists of a mean-square reconstruction error term and a regularization term on the norm of the parameters.

The reconstruction of the observation from a sparse linear combination of the elements of the dictionary can be expressed as a convex optimization problem, where the sparseness on the solution is achieved by the regularization term. The amplitudes of the elements of the dictionary will be mostly zero, except the weights $\alpha_{i,j}$ of the atoms (see equation (4)) that best approximate the value of the VTEC at the pierce points.

The dictionary does not need to be composed of orthogonal elements but can be any arbitrary set of elements, in particular, a set of elements that is adapted to the problem at hand. The atomic decomposition has several additional properties that are useful, namely, (a) in addition to dealing with Gaussian noise, one can also deal with noise of other origins that might introduce a large distortion on some of the samples (see Appendix A2); (b) allows for a natural way of dealing with the nonuniform sampling process; and (c) provides an objective criterion for determining the number of MSTIDs. The formal model of the MSTIDs (i.e., the parametric description) is presented in section 5, equations (5) and (7).

5. Construction of the Dictionary and Estimation Criteria

In this section, we will present (a) the model of the MSTID and the design of the dictionary (see section 5.1), (b) the definition of the loss function and regularization criteria (see section 5.2), and (c) the method that computes the sparse decomposition and implementation aspects (see section 5.3).

The dictionary is designed from a model that assumes that the pierce point observations $V(x, y)$ at epoch t can be expressed as a linear combination of several MSTID waves $T_i(x, y)$, as in equation (5). The parameters α_i for epoch t are estimated from the reconstruction error only at the set of pierce points $I_{x,y}$. Thus, for a map containing M MSTIDs we have

$$V(x, y) = \sum_{i=0}^{M} \alpha_i T_i(x, y) + n(x, y) \tag{5}$$

The coordinates x and y are coordinates on the map (note that although the model is for the whole region, only the IPP coordinates are used in the estimation process), the dictionary atom $T_i(x, y)$ models the wavefront snapshot of one MSTID wave at epoch t. The term $n(x, y)$ is an additive random noise, and α_i is the parameter to be estimated, which represents the amplitude of the ith MSTID.

We will define the vector of amplitudes at epoch t, as $\alpha_t = [\alpha_1, \alpha_2, \alpha_3, \ldots, \alpha_N]$, where N is the size of the dictionary. The number M of MSTIDs is much smaller than the number of elements of the dictionary N.

5.1. Design of the Dictionary

The model consists of the superposition of several planar monochromatic waves from a dictionary of elements $T_i(x, y)$. We will model the MSTID $A(x, y, t)$ as a 2-D monochromatic planar wave such as

$$A(x, y, t) = A_0 \cos\left(\vec{k} \cdot (x, y) - \omega(t - t_0) + \varphi_0\right) \tag{6}$$

where $\vec{k}$ is the 2-D angular wave number vector, with the module $\left|\vec{k}\right| = \frac{2\pi}{\lambda}$; λ is the wavelength and the normal vector $\frac{\vec{k}}{\left|\vec{k}\right|} = (\cos\theta, \sin\theta)$ points in the direction of propagation of the wave. The wave amplitude is A_0. The terms ω, t_0, and φ_0 are the angular frequency, the starting epoch, and initial phase of the MSTID wave, respectively. The ith dictionary element $T_i(x, y)$ at epoch t is defined as follows:

$$T_i(x, y) = \cos\left(\frac{2\pi}{\lambda_i}\left(x\cos\theta_i + y\sin\theta_i\right) + \varphi_i\right) \tag{7}$$

The element $T_i(x, y)$ of the dictionary is characterized by λ_i wavelength, φ_i phase, and θ_i wave azimuth. The parameters of each element of the dictionary (θ, λ, and φ) are quantized as real numbers, with values restricted to realistic ranges.

The dictionary D is constructed by the concatenation of the set of N elements $T_i(x, y)$, reshaped as vectors, giving an array D, defined as $D = [T_1, T_2, T_3, \ldots, T_N]$. The elements $T_i(x, y)$ are generated by assigning to the parameters $\{\lambda, \theta, \varphi\}$, all possible feasible values in a quantized range. Each element $T_i(x, y)$ consists of a grid of P_v rows and P_h columns, i.e., a uniform sampling of the geographical region of interest. Then, the array is reshaped to a vector T_i of dimension $P_v \times P_h$. Note that the observations correspond to the IPPs; hence, in the estimation of the vector, α_t will be done only with the coordinates (x, y) corresponding to measured IPPs.

5.2. Loss Function and Regularization

Here we will analyze the criterion for estimating the parameters α_t, by means of a trade-off between a loss function (i.e., how well we approximate the observations by means of the model) and a regularization term (i.e., constraints on the possible solutions).

The loss function term implicitly expresses our assumptions about the statistics of the estimation error. We define our loss function as the logarithm of the likelihood function, i.e., the logarithm of the joint probability of the observations given the parameters to be estimated. We assume that the probability of the model depends exponentially on the norm ℓ_p of the difference between the observed values and the values generated by our model. Also, we introduce in the model a regularization term which allows for expressing desirable properties of the solution. In our case, as we want sparsity on the solution; we will penalize certain

distributions of values of the estimated vector of parameters α_t by means of a norm ℓ_q. Therefore, the general form of the problem to solve can be expressed as

$$\min_{\alpha_t} \|V - D\alpha_t\|_{\ell_p}, \qquad \text{subject to} \quad \|\alpha_t\|_{\ell_q} < \tau \tag{8}$$

where V consists of the IPP observations, D is the dictionary for reconstructing the observation at the pierce points, α_t is the vector to be estimated at time t, and ℓ_p and ℓ_q define the norms that are applied to each term of the optimization problem. Note that the norm of the reconstruction error ℓ_p is different from the norm ℓ_q of the regularization term. The above expression can be written in the Lagrangian form as

$$\alpha_t^{\star} = \arg\min_{\alpha_t} \frac{1}{2}\|V - D\alpha_t\|_{\ell_p} + \rho\|\alpha_t\|_{\ell_q} \tag{9}$$

There is a one-to-one correspondence between the parameter τ in (8) and ρ in (9); see *Hastie et al.* [2009] for details. The arguments for selecting the values of each norm are discussed in detail in sections 5.2.1 and 5.2.2.

5.2.1. Loss Function

The metric ℓ_p in the loss function is equivalent to assuming a particular probability distribution of the reconstruction error in equation (8). In particular, the term $\|V - D\alpha_t\|_{\ell_p}$ can be interpreted as the logarithmic likelihood of an exponential distribution. The metrics that we considered were the following:

1. $\ell_p = \ell_2$ assumes a multivariate Gaussian distribution; thus, the logarithmic likelihood function is the sum of the squares of reconstruction errors. Note that this criterion penalizes quadratically the error, so sample points where the reconstruction error is significant will have a large impact on the estimation of the parameters α_t. That is, the solution will be very sensitive to values far from the mean.
2. $\ell_p = \ell_1$ assumes a multivariate Laplacian; thus, the logarithmic likelihood function is the sum of the absolute values of the errors on the data. The key point is that this distribution assumes that important deviations in the reconstruction error are more likely than the case of a Gaussian distribution; therefore, the penalization is lower, and the impact of large errors in the estimation of the parameters α_t is lower.

For the selection of the norm ℓ_p, we considered the following fact. The solution to the problem posed by equation (8) is especially sensitive to the norm ℓ_p, because of the geometry of the pierce points. This is because as the points are not uniformly distributed over the plane, the IPPs follow a pattern that consists of the projection of the ground stations to the effective height viewed from the satellite. The consequence is a bias in the detection of the directions of the waves imposed by the geography of the network. This bias is a consequence of the elongated distribution of receivers and the regions with the highest density of receivers, which make the outliers dependent on the azimuth of the MSTID.

As a result, the contribution to the reconstruction error of the receivers located on the border of the network will be larger than those in the central part of the network. This is because small errors in the estimation of the propagation azimuths will be enhanced over long distances (i.e., NE and SW extremes). That is, a leverage effect will appear due to the geometry and distribution of the receivers.

If we assume a ℓ_1 penalty for the reconstruction error, the outliers have a lower impact in the estimation compared to the case of ℓ_2. Therefore, as we want an estimator that is sensitive to the small deviations of the estimated angle of the MSTID (i.e., leverage effect), we selected ℓ_2 for the loss function. In this way, a small error in the estimation of the angle will result in a larger contribution to the total error of the IPP located at the extreme points of the network and therefore will have a high influence in the final estimation. Another aspect of the estimation of the data is that we would like to impose sparsity in the solution by means of the regularization term; in this case, the requirements on the norm are inverted.

5.2.2. Regularization Term

The dictionary D is designed to be redundant and with highly correlated elements, in order to detect a specific family of waveforms. We would like to solve the approximation problem summarized in equation (8) using the least number of elements of the dictionary, i.e., a sparse solution in the space of the parameters α_t. This can be done in principle by means of the pseudometric ℓ_0, which minimizes the number of elements different from zero regardless from their value. For a discussion about why ℓ_0 is a pseudometric, see *Hastie et al.* [2015]. The problem to be solved can be stated as follows:

$$\min_{\alpha_t} \|\alpha_t\|_0, \qquad \text{subject to} \quad \|V - D\alpha_t\|_2 \leqslant \varepsilon \tag{10}$$

where ε represents the permissible deviation of the representation $D\alpha_t$ from the global IPP measurements of the VTEC map $V(x, y)$. Unfortunately, this problem is not convex and can only be solved by combinatorial methods, which for the number of unknowns in the problem at hand is computationally unfeasible.

In this section, we argue that the most adequate norm for the regularization term is ℓ_1. The objective is to select the smallest subset of uncorrelated elements of the dictionary while minimizing the reconstruction error on a dictionary of redundant and nonorthogonal elements that spans the space of possible solutions.

The use of norm ℓ_1 gives rise to sparse solutions in the linear regression (see *Hastie et al.* [2015] for a geometrical explanation) and under certain situations is a good approximation of the pseudonorm ℓ_0, which explicitly minimizes the number of terms different from zero. The use of norms ℓ_p, with $p < 1$, increases the sparsity, but the resulting problem is not convex any more, and therefore, the techniques of convex programming cannot be used. Consequently, for this problem, we will use the ℓ_1 norm as a regularizer on the parameters. Note that in Appendix A3, we introduce an iterative solution using ℓ_1 that indirectly approximates the norm ℓ_p, with $p < 1$, in order to obtain a more sparse solution.

The technique that fulfills all the requirements is the LASSO [see *Hastie et al.*, 2015] which is stated as an optimization problem that minimizes the square of the reconstruction error, with a regularization norm on the weights based on ℓ_1. This is the technique that was selected for the estimation of the MSTIDs.

A related technique is the elastic net [see *Hastie et al.*, 2015, chap. 4], which is a convex combination of the ℓ_1 and ℓ_2 norms on the regularization term. In contrast to LASSO, this technique assigns nonzero values to correlated elements of the dictionary. But in our case, the dictionary consists of highly correlated atoms, because the elements consist of a fine-grained enumeration of the parameters of the wavefronts. In our preliminary experiments, we found that the elastic net yielded poor performance; therefore, it was discarded. On the other hand, the use of only the ℓ_1 norm on the regularization term gives a crisp solution assigning the resources to only clearly distinct elements, which is compatible with our initial hypothesis that there is only a limited number of distinct MSTIDs.

Finally, to solve an ambiguity that might arise in the estimation coefficients α_t, we impose the solution to be in the first quadrant, that is that all the elements of the vector α_t should be positive. This is justified by the interpretation of coefficients α_t as amplitudes for each existing MSTID and by the fact that changing the sign of an element of the vector α_t that multiplies the elements of the dictionary $T_i(x, y)$ (see equation (7)) equals a change in the phase φ_i of 180°.

5.3. Parameter Estimation: The LASSO Solution

Finally, the components of the MSTIDs are obtained by solving an optimization problem with a term on ℓ_2 for the reconstruction error and a term on ℓ_1 for the regularization term. This can be stated as the following:

$$\hat{\alpha}_t = \arg\min_{\alpha_t} \frac{1}{2}\|V - D\alpha_t\|_2^2 + \rho\|\alpha_t\|_1 \tag{11}$$

The sparseness of the solution will depend on an independent parameter ρ which has to be adjusted as explained in Appendix A1. Empirically, we have found a low sensitivity of the sparseness with respect to the parameter ρ, since the number of active elements of the dictionary is piecewise constant for wide margins of ρ. Also note that in the final implementation, we iterated the above equation as shown in Appendix A3.

5.4. MSTID Detection and Velocity Estimation

For a given snapshot, the solution to equation (11), even if no MSTIDs are present, will always find a set of parameters α_t that minimize the approximation of the VTEC map V in terms of the dictionary D. Therefore, to decide the presence of MSTIDs, we used two criteria, (a) continuity of the parameters in a sliding window of 20 snapshots (600 s) and (b) the value of ρ.

The continuity of parameters was decided inside the window of 20 snapshots (i.e., 600 s) to reduce the rate of false detections. Additionally, this allowed for having enough samples of phase φ for computing the velocity. The continuity criterion consisted of setting the variation of parameters between the snapshots within the following ranges: azimuth $\Delta\theta = \pm 5°$ and wavelength $\Delta\lambda = \pm 10$ km. To decide that a MSTID was present, the length of continuity had to be greater than 600 s. Thus, the tracking of the MSTID between consecutive snapshots allowed for a slow drift in the parameters with time.

The value of ρ is crucial for making the method work. A property of the LASSO that arises from the use of ℓ_1 in the regularization term of equation (11) is that the number of elements in α_t that are different from zero is constant for a large margin of variation of ρ [see *Hastie et al.*, 2015, chap. 1]. Therefore, the number of elements of α_t different from zero is constant inside large margins of the value of ρ. Empirically, we have determined that values of ρ in the low margin are associated with the absence of MSTIDs. This was determined by visual inspection of the maps and by a lack of continuity of the parameters of the MSTID. The strategy that we followed for determining the number of distinct MSTIDs was to solve equation (11) for an initial value that detects no MSTIDs and reduce the value of ρ iteratively by 0.8 at each step. Once a set of several MSTIDs were determined in a stable subrange of the margin, we applied the reweighting method that determines an approximation to a ℓ_0 solution, i.e., minimizing explicitly the number of elements different from zero that yield the best approximation (see Appendix A3).

The estimation of the velocity is dependent on the continuity tracking of each MSTID, because it is derived from the slope of the phase φ (see Appendix A1). Note that phase φ from each snapshot is in a different horizontal coordinate system, taking the center of mass of the pierce point set as the origin. This center of mass varies from one snapshot to the next (see section 2.2); therefore, the phase φ has to be updated by changing into a unified coordinate system. Moreover, the noise estimation of the phase φ translates into higher uncertainty in the estimate of the slope. Also, when the continuity in the tracking is broken, even in small gaps, the error on the estimate of the slope can be extremely high. Dealing with issues of the increase of the estimation errors and outliers is critical for the correct estimation of the velocity. Thus, the estimate of the velocity is performed from the slope of the phases φ of each MSTID, by means of the regression method that is robust to the presence of outliers, such as the Random Sample Consensus (RANSAC) method [see *Fischler and Bolles*, 1981]. The use of the RANSAC method is key for obtaining good estimates of the velocity.

The details of the implementation and design choices of the algorithm are discussed in Appendices A1 – A3. The details are important to be able to reproduce the experiments and also to understand some implementation choices that make the method more accurate and less computationally expensive.

6. Experiments

In this section, we test the performance of the algorithm in two situations, (a) simulated data in a realistic scenario, i.e., GNSS data, which are a superposition of several preset modeled MSTID waves and noise and distortions of different origins, and (b) actual dual-frequency carrier phase GNSS measurements on a given representative day for all the stations, i.e., GNSS data from GEONET on the 80th day of 2011. For comparison purposes, we will present as benchmarks the estimated MSTIDs with the comprehensive GNSS Ionospheric Interferometry (cGII) technique [see *Hernández-Pajares et al.*, 2012].

6.1. Evaluation of the ADDTID Algorithm on a Simulated Scenario

To test the ADDTID algorithm, we simulated three simultaneous MSTIDs at real IPP locations, measured on the 80th day of 2011. The simulation was based on the measurements of the detrended VTEC maps in *Hernández-Pajares et al.* [2006] and were generated following the model in equation (7) in section 5.1, using a realistic set of parameters.

The experiment consists of a temporal sequence of the detrended VTEC maps affected by three different MSTID waves which are occurring at the same height (250 km, to make the experiment compatible with the estimate with real data; for justification, see the beginning of section 6.2). The parameters of the three waves are summarized in Table 1. The values of the azimuths and amplitudes were selected to generate a pessimistic scenario, i.e., similar azimuths, one of them almost 180° with respect to the others, and a ratio of amplitudes of 1/3 between the main MSTID and the smallest. To simulate the parameter drift as a function of time in the real waves, we fixed an initial value which was perturbed cumulatively by a random percentage at each snapshot; that is, we created Brownian motion of the parameters. This drift percentage was 0.1% for the wavelength, 0.5% for the velocity, and 0.5% for the azimuth and was selected following a subjective criterion of visual similarity between the simulated evolution of the maps and the real maps.

In addition, it should be remarked that the introduction of this drift allows for testing the performance of the system, when the parameters of the MSTID do not correspond exactly to the values of the elements of the dictionary. This last point should be emphasized for two reasons. The first is related with modeling realistic drifts in time in the features of the maps, while the second is related with the methodology. It is highly

Table 1. Parameters of the MSTID in the Simulated Experiment

TID Waves	Amplitude (TECU)	Wavelength (km)	Velocity (m/s)	Azimuth (deg)
$T_1(x,y)$	0.3	91.58	150.50	76
$T_2(x,y)$	0.6	156.71	90.77	275
$T_3(x,y)$	0.9	254.85	200.21	124

improbable that the dictionary will contain parameters that match exactly the parameters of a real MSTID. This methodological aspect is important, because we have checked experimentally that when the parameters of the dictionary coincide with the values of the wave to be estimated, the ambiguity with the value of φ is much lower, which would show unrealistically good performance.

To simulate a multiplicative distortion, which could be related among other reasons to the elevation angle and loss of measurements from one station and cycle slips, we decided to take the most pessimistic approach, which consisted of the substitution of the value at the partial pierce points of a given satellite with Gaussian noise, as shown in equation (12).

Therefore, using the same locations of the measured IPPs $I_{x,y}$ at each epoch t, the time series of the detrended VTEC $V_s(x,y)$ was created as follows:

$$V_s(x,y) = \begin{cases} \sum_{k=1}^{3} T_k(x,y) + n(x,y) & \text{, if } (x,y) \notin R_{x,y} \\ n(x,y) & \text{, if } (x,y) \in R_{x,y} \end{cases} \tag{12}$$

where $n(x,y)$ is the random Gaussian noise term set at SNR = 0 dB. In addition, 10% of the IPPs of each satellite (set denoted as $R_{x,y}$) are left with no MSTID activity to account for the above mentioned multiplicative distortion. The MSTID activity maps were constructed from the simulated GNSS data $V_s(x,y)$, and the estimation of the number of MSTIDs and the parameters of each MSTID at a given snapshot was done by means of the method presented in Appendices A1 – A3.

The resulting scatterplot in polar coordinates (azimuth versus velocity) is shown in Figure 3. The simulation spanned a 24 h period, using real IPPs of all satellites, i.e., comprising the same IPPs and elevations as the real data. Figure 3 shows that three MSTIDs are detected. The value of the azimuth corresponding to each MSTID is estimated almost exactly; nevertheless, the velocity estimate has a higher variability. For the simulation we selected a SNR = 0 dB, which explains that the variability of the velocity is higher than that estimated from the

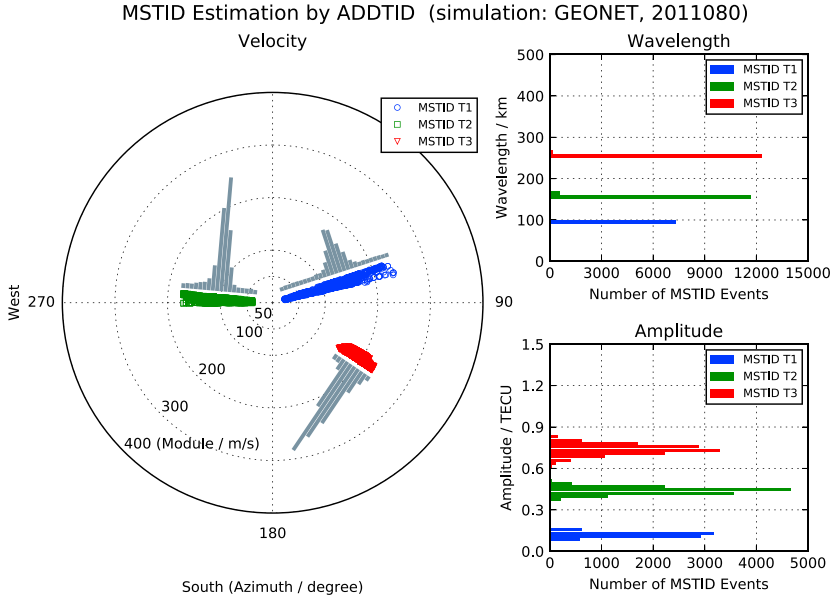

Figure 3. (left) Polar plot (velocity versus azimuth) of the estimated MSTIDs (histogram of the velocity module superimposed on the plot) and histograms of the estimated (top right) wavelengths and (bottom right) amplitudes; the GNSS observation data were simulated from GEONET, for all the satellite PRNs, on the 80th day of 2011.

real data. This SNR was selected to test the robustness of the method in adverse conditions. Also, the low SNR in the simulation affected all satellites equally, while for the real data, the SNR depends on the elevation of the satellite. In the same Figure 3, we present the histogram of the velocities, and the mode of the histograms is near the real value. Note that even though the $T_1(x, y)$ MSTID had the lowest amplitude and the angle was selected so that it was almost 180° with respect to the $T_2(x, y)$, its parameters could be estimated correctly. On the other hand, the variability in the estimation of the velocity of $T_3(x, y)$ had a much lower variability in the estimation.

The histograms of the wavelength and amplitude estimations are presented in Figure 3 (right column). The estimate of the wavelength was as accurate as the estimate of the azimuth. On the other hand, the value of the estimated amplitude presented a systematic downward bias, preserving the relative ranking. This downward bias on the estimation of the detrended VTEC is due to the regularization term in equation (11) and is inherent to the algorithm. Note that in both cases, the variability of the estimation is small. The number of MSTIDs is determined correctly, in the sense that there were no false MSTIDs. The determination of the number of MSTIDs present was conducted using the reweighted LASSO (see Appendix A3 for details and justification). The initial estimate of the LASSO gives several candidates that might be very similar, and the process of renormalization combines the candidates that are compatible with the hypothesis of a unique wave. Also, it should be emphasized that the number of MSTIDs to be detected is a free parameter, and the algorithm finds the total number of MSTIDs along with their parameters.

6.2. MSTID Estimation From Real Dual-Frequency Carrier Phase GNSS Data: Results and Discussion

In this section, we test the method on real GNSS data from the GEONET in Japan. We selected the 80th day of 2011 (i.e., 21 March, the first day after the vernal equinox), because it exhibits a rich typology of MSTIDs that might show the frequent winter-like daytime characteristics [*Kotake et al.*, 2007], nighttime propagation excited by solar terminator [*Afraimovich et al.*, 2009], and summer-like propagation in the whole day [*Oinats et al.*, 2015]. There were no disturbances originated by phenomena such as major geomagnetic storms, solar flares, significant earthquakes, tsunamis (no corresponding ionospheric disturbances in the GEONET-observing region recorded in *U.S. Department of Commerce* [2011a, 2011b, 2011c]), or strong geomagnetic activities (the planetary 3 h range index $kp \leq 3$) [see *U.S. Department of Commerce*, 2011d]. Moreover, the hourly height distribution of peak electron density (h_mF_2) on this day was from 250 km to 350 km (the h_mF_2 data of the International Reference Ionosphere 2012 model (IRI-2012) [see *Bilitza et al.*, 2014], obtained from *National Aeronautics and Space Administration/Goddard Space Flight Center (NASA/GSFC)* [2012]). According to *Hernández-Pajares et al.* [2006], the maximum MSTID generation occurs at the height below h_mF_2 because the MSTIDs are generated by the interaction between the neutral and ion particles. We assumed that the most frequent dominant MSTIDs are generated below h_mF_2, so we took 250 km as the mean effective height of the MSTIDs, which is lower than the average h_mF_2 of 290 km.

In the following sections, we apply the ADDTID algorithm to real dual-frequency carrier phase GNSS data of GEONET, and for the March equinox we present the following results: (a) the detection and estimation of the parameters of simultaneous MSTIDs at daytime and nighttime (see 6.2.1), (b) the detection of several MSTIDs that propagate in the same direction but with different wavelengths and velocities (see 6.2.2), (c) the detection of several MSTIDs that propagate in opposite directions (see 6.2.3), and (d) the detection of circular waves (see 6.2.4).

6.2.1. Characterization of Multiple MSTIDs at Daytime and Nighttime

In this section, we present the estimation results in two scenarios, (a) performance of the ADDTID method at noon, and at midnight for a single satellite, and (b) MSTID characteristics throughout the day, in intervals of 24 h, for all the satellites. In each case, we give a discussion of the results.

In the first scenario we examine the performance at the two periods of the day, i.e., between 10:00–12:00 LT (for satellite PRN 5) and 1:00–3:00 LT (for satellite PRN 7). Satellite PRN 5 was selected because it presented several simultaneous MSTIDs with similar amplitudes, while satellite PRN 7 was selected to illustrate the case of the detection of simultaneous MSTIDs when one MSTID had an amplitude significantly higher than the other.

By visual inspection, one can see in Figures 2a–2d that the maps (at around 11:00 LT for satellite PRN 5) show the interference pattern of several simultaneous 2-D MSTID waves. In these maps, one can measure two dominant MSTIDs that propagate in the equator-east and equator-west directions, with wavelengths of about

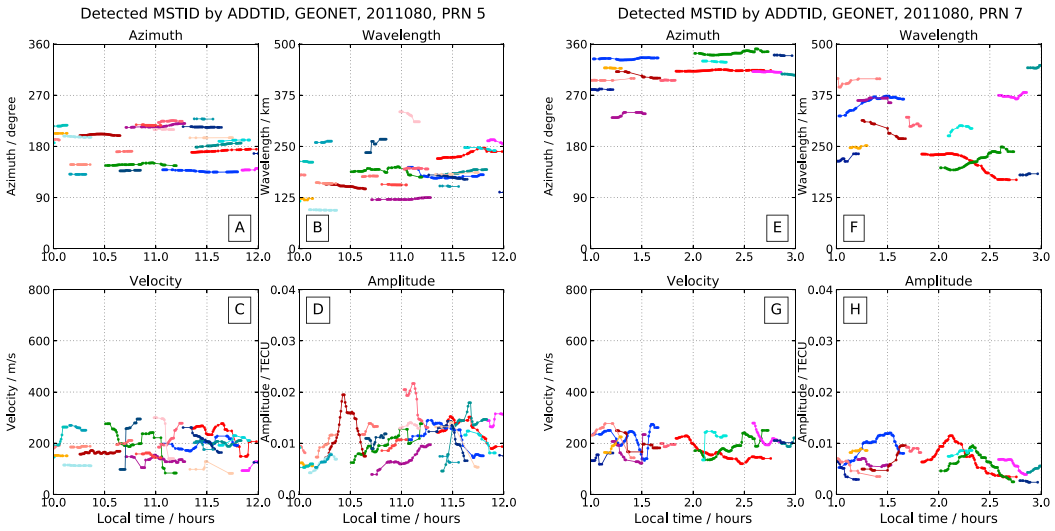

Figure 4. Time evolution of the MSTID estimates of azimuths, wavelengths, velocities, and amplitudes at local noon and midnight from the GEONET network, on the 80th day of 2011. (a–d) The time evolution of the MSTID estimates at the local noon (10:00–12:00 LT) for satellite PRN 5. (e–h) The time evolution at the local midnight (1:00–3:00 LT) for satellite PRN 7.

135 km and 180 km and velocities of 150–200 m/s and 200–250 m/s, respectively. The maps in Figures 2e–2h show a predominant MSTID wave that propagates in the northwest direction with wavelength between 250 and 300 km and a velocity between 125 and 200 m/s. In the daytime case, the MSTID waves had similar amplitudes, which gave rise to the interference pattern, but in the nighttime case, at a given time one MSTID had an amplitude significantly higher than the others. The results given by the ADDTID algorithm are compatible with the visual analysis. In Figure 4, we show the time evolution of the estimates by means of the ADDTID algorithm of the MSTID parameters for satellite PRN 5 (Figures 4a–4d) and satellite PRN 7 (Figures 4e–4h). Each individual MSTID is identified by a color code. Figures 4a–4d show the evolution of several MSTIDs during the time interval from 10:00 to 12:00 LT. The azimuth time series shows the overlap and continuity of different MSTIDs, having up to three different MSTIDs at different moments. Figures 4e–4h show the evolution at nighttime for satellite PRN 7. The ADDTID algorithm, in addition to detecting the predominant MSTIDs, also detects at times two or three different MSTIDs. The predominant MSTIDs is consistent with the azimuth seen visually at Figures 2e–2h. Also, note that the algorithm is able to follow drifts in the parameters of the MSTIDs as a function of time.

The second scenario is summarized in Figure 5, where we show the time evolution (0:00–24:00 LT) of the MSTID parameters: azimuth, wavelength, velocity, and period, estimated by the ADDTID method. Each MSTID is identified by a different color code, and the amplitude is coded by the size of the points (i.e., the larger the size, the higher the amplitude). In Figure 5 we show the time evolution of the velocity of each MSTID. The algorithm is able to track the slow changes of the velocity with continuity. Likewise, the period of the MSTIDs shows also a slow continuous change for each individual MSTID, but during nighttime the different MSTIDs show a collective high variability in the range of 500–2700 s.

In Figure 6 we compare the results of the ADDTID method with the cGII method for the case of the azimuth. The MSTID estimates by means of the cGII method were performed from eight subsets of GEONET stations, which are indicated by blue dots in Figure 1 (left). Note that the ADDTID method allows the detection of individual MSTIDs by introducing continuity constraints, which greatly reduces the estimation noise. The MSTIDs time series can also be characterized by means of the azimuth versus velocity polar plots at intervals of 1 h, as shown in Figures 7 (ADDTID) and 8 (cGII). The results of both models are consistent in terms of directions and intensities. The main difference was that the ADDTID detects the azimuths of each MSTID with a much lower dispersion and that MSTIDs with similar azimuths can now be distinguished. A difference between the intensities shown in the figures resides in the fact that the ADDTID estimates individual amplitudes, which are coded by the color intensity of the dots. In the case of cGII, the information related to the intensity of the MSTID is the root-mean-square of the detrended VTEC of all satellites, i.e., Single Receiver Medium-scale

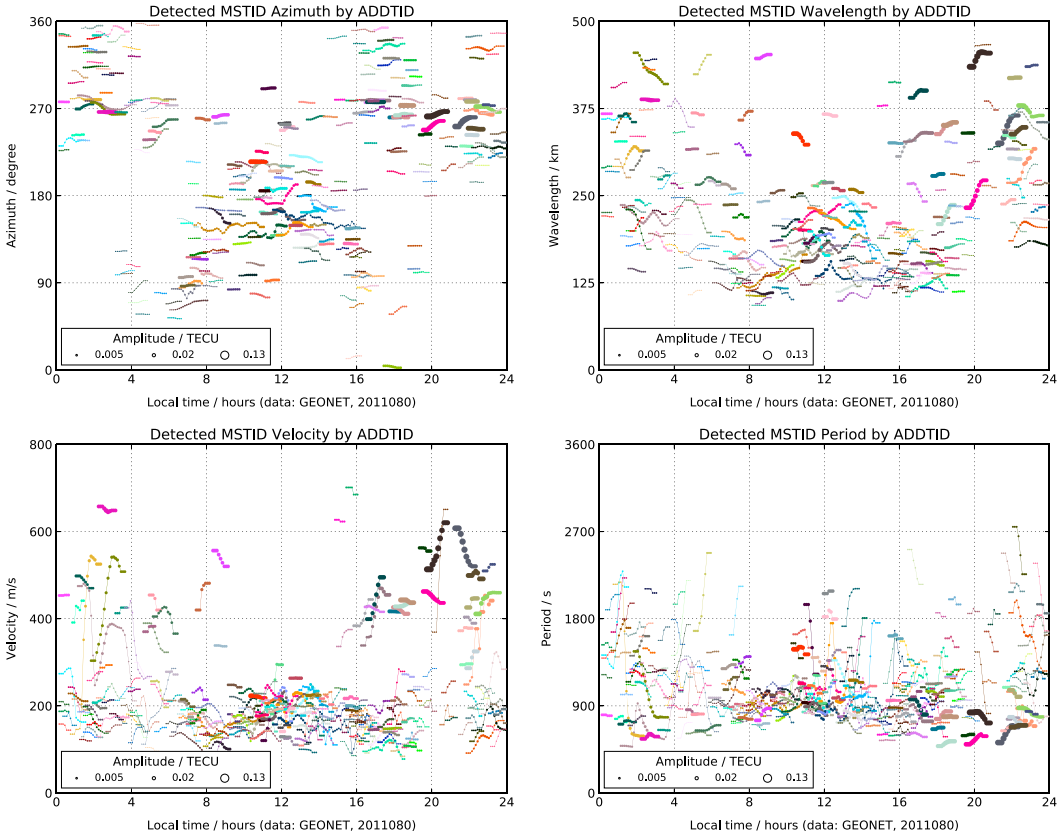

Figure 5. Time evolution (0:00–24:00 LT) of the (top left) estimates of azimuth, (top right) wavelength, (bottom left) velocity, and (bottom right) period of the MSTID propagation estimated by means of ADDTID. The individual MSTIDs are color coded, and the amplitude is represented by the size of the points, from the GEONET network for all GPS satellites, on the 80th day of 2011.

Traveling Ionospheric Disturbance (SRMTID) index (see for details *Hernández-Pajares et al.* [2012]), which is coded by the color intensity of the dots. The apparent dispersion of velocity seen in the two figures is due to the fact that the velocity of the MSTIDs changes in a continuous way during the time interval corresponding to the plots.

Discussion. The distribution of the MSTID estimates follow typical daytime and nighttime patterns of the March equinox. During the daytime, especially near local noon (8:00–16:00 LT; see Figures 2a–2d, 5, and 7), the ionospheric activity is at the maximum level. More than 10 simultaneous MSTIDs were detected by the ADDTID method. These MSTIDs presented amplitudes in the range of 0.02–0.1 TECU, with azimuth directions from

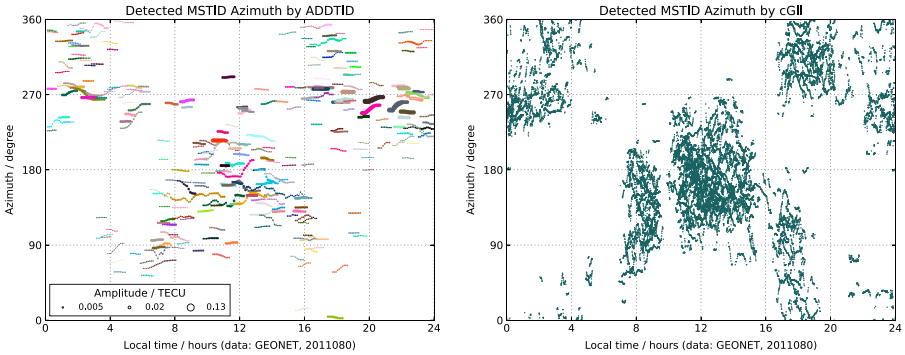

Figure 6. Time evolution (00:00–24:00 LT) of the estimates of azimuth, for the GEONET network. (left) ADDTID and (right) cGII. GEONET network for all GPS satellites, on the 80th day of 2011.

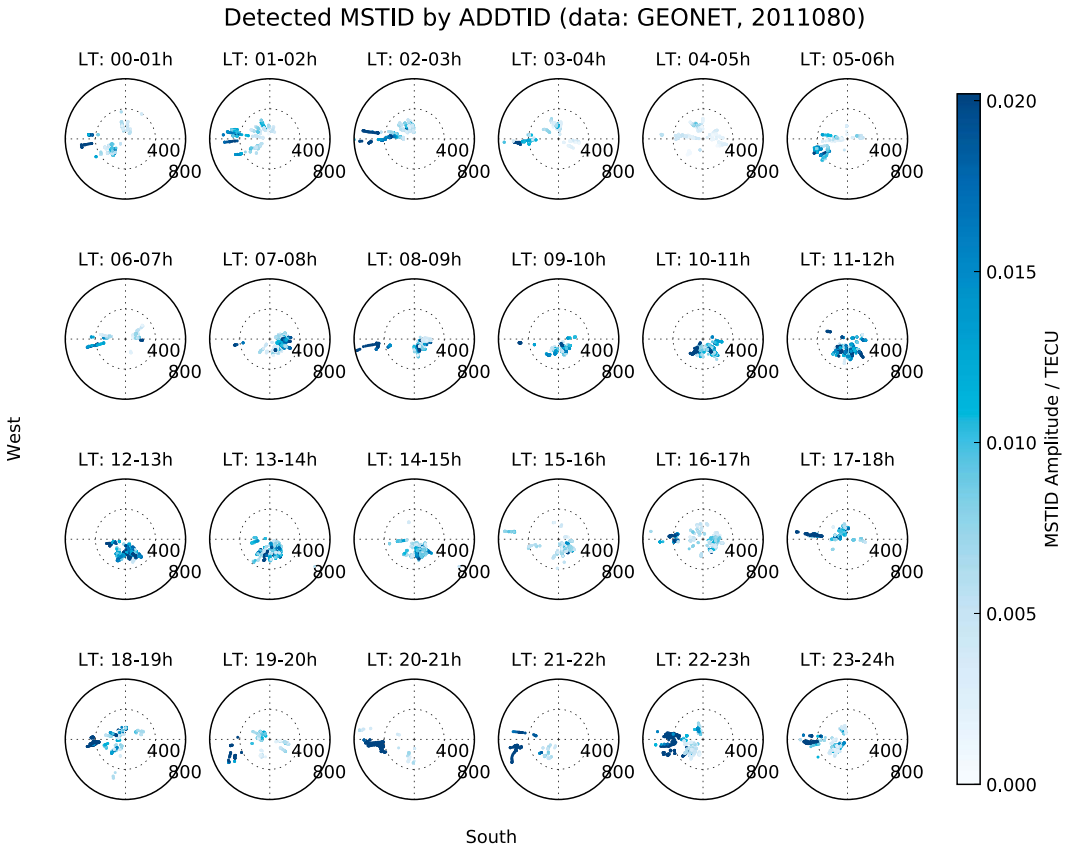

Figure 7. Intensity polar plots of the MSTIDs, velocities (in m/s), and azimuths (in degree) for the whole day detected by ADDTID; the color intensity is weighted by the MSTID amplitude (in TECUs), by local hour, from the GEONET network for all GPS satellites, on 80th day of 2011.

north to the equator/equator-east, velocities in the range from 100 m/s to 300 m/s, the wavelengths in the range of 120–250 km, and periods in the range of 600–2000 s. The daytime behavior of the MSTIDs in the March equinox agree with the daytime MSTID behavior in the winter, as mentioned in *Hernández-Pajares et al.* [2012]. These similarities are also mentioned in *Otsuka et al.* [2011] (GEONET) and *Kotake et al.* [2007] (California GPS network).

In contrast with the daytime, the MSTID activity is weaker and more irregular during the rest of the day. This is due to the smaller overall intensity of the MSTIDs at nighttime and during the morning/evening solar terminator as shown in Figure 5. During nighttime (i.e., 00:00–04:00 LT and 20:00–24:00 LT), the amplitudes of the dominant MSTIDs are in the range of 0.005–0.13 TECU. From the features of the distribution of the parameters of the MSTID shown in Figure 5, one can categorize the nighttime MSTIDs into two types: the weak nighttime MSTIDs with amplitude in the range 0.005–0.02 TECU and the strong nighttime MSTIDs in the range of 0.02–0.13 TECU. The weak nighttime MSTIDs, accounting for 80% of the total estimated nighttime MSTIDs, propagate all westward direction (southwestward/westward/northwestward), with velocities in the range of 100–250 m/s. This is consistent with the nighttime MSTID behavior in summer [see *Hernández-Pajares et al.*, 2012]. The wavelengths were in the range of 150–450 km and show a much higher variability than in summer (50–250 km) [*Hernández-Pajares et al.*, 2012]. The range of the estimated wavelengths is consistent with the range 150–500 km in winter/summer as mention by *Tsugawa et al.* [2007a]. The characteristics of weak nighttime MSTID propagation are compatible with the case study of nighttime MSTIDs in equinoxes for midlatitude mentioned in *Otsuka et al.* [2011] and *Oinats et al.* [2015]. The above mentioned properties are summarized in the detrended VTEC maps in Figures 2e–2h and in the estimates as shown in Figures 5 and 7 [*Hernández-Pajares et al.*, 2012].

The strong nighttime MSTIDs have higher velocities, shorter periods, and weaker velocities than their weaker counterparts. The strong nighttime MSTIDs have a higher amplitude up to 0.13 TECU. The wavelengths have

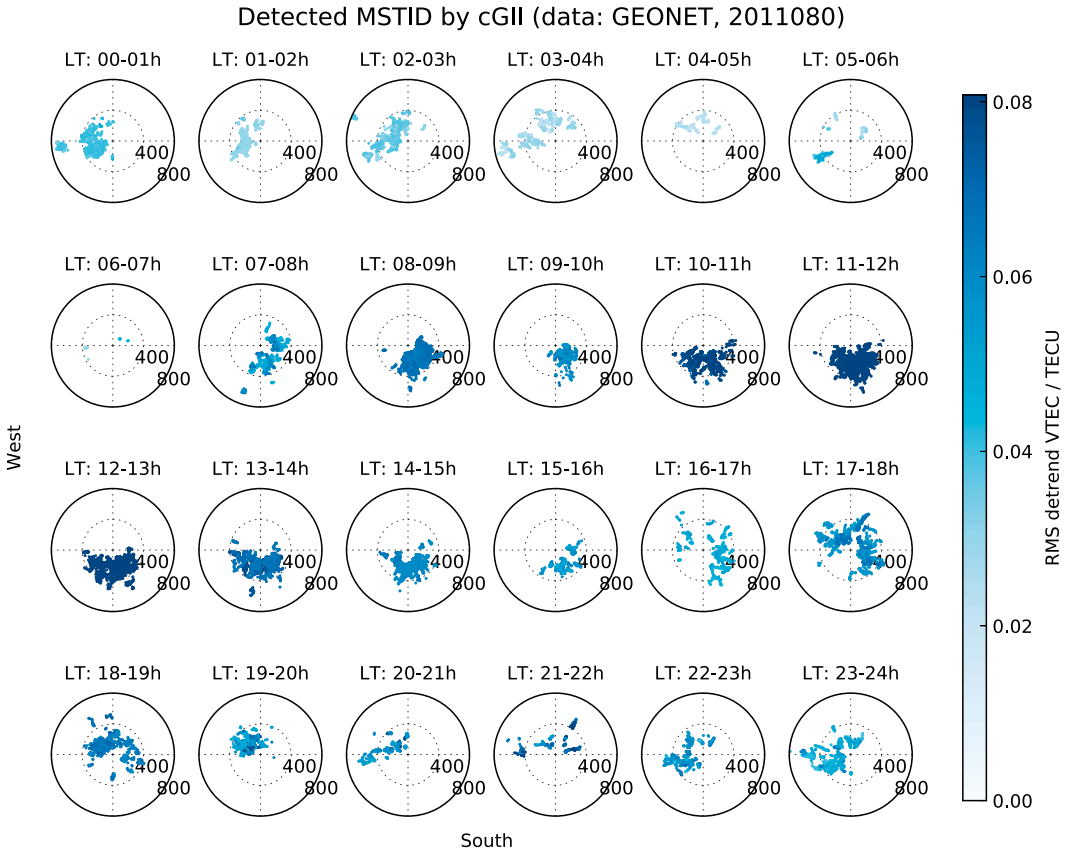

Figure 8. Intensity polar plots of the MSTIDs, velocities (in m/s), and azimuths (in degree) for the whole day detected by cGII; the color intensity is weighted by the RMS detrended VTEC (in TECUs) from the visible satellites, by local hour, from the GEONET network for all GPS satellites, on 80th day of 2011.

a much higher mean and dispersion and the velocities present in the range of 400–600 m/s as can be seen in Figure 5. This feature of the velocity component appears in the results of both methods, ADDTID and cGII. See, for instance, Figures 7 and 8. Figure 9 shows the time interval between 20:00 and 21:00 LT, where two MSTIDs are found with velocities over 400 m/s. This range of velocities is compatible, with *Deng et al.* [2013], where they report a fast MSTID in the local morning (about 8:00 LT) propagating from east to west across Germany with a velocity of about 700 m/s, a period of 420 s, and a wavelength of 302 km.

During the morning and evening solar terminators (04:00–08:00 and 16:00–20:00 LT), the MSTIDs occur simultaneously in both directions (equator-eastward and westward, respectively), as shown in Figure 5. During the morning terminator, the westward MSTIDs are weaker, while the MSTIDs toward equator-east are stronger. The evening pattern shows the opposite behavior. These features are also mentioned by *Kotake et al.* [2007] and *Otsuka et al.* [2011] for dominant MSTIDs propagation during the morning/evening solar terminator introduced in the California GPS network. The explanation is that the MSTIDs of the morning/evening solar terminator propagate in the direction contrary to the direction of the neutral winds, which always blow from dayside to the nightside. Another compatible observation of the equinox MSTIDs [see *Afraimovich et al.*, 2009] are of magnetohydrodynamic (MHD) nature and are produced immediately after evening solar terminator.

6.2.2. Different MSTIDs That Propagate in Almost Identical Azimuths

Figures 9a–9d show the presence of two different MSTIDs with the same azimuth and different wavelengths and velocities. To show more clearly the superposition of both waves, we projected the detrended VTEC in the direction given by the estimated azimuth, which is plotted superimposed on the figure in purple.

Discussion. Both MSTIDs (20:00–21:00 LT) propagate in the west/equator-west direction, with a similar velocity of about 500 m/s but with wavelengths of about 450 km and 250 km. From these figures, one can see that the dominant MSTID has a wavelength of 450 km. The resulting projected waveform follows the form of the

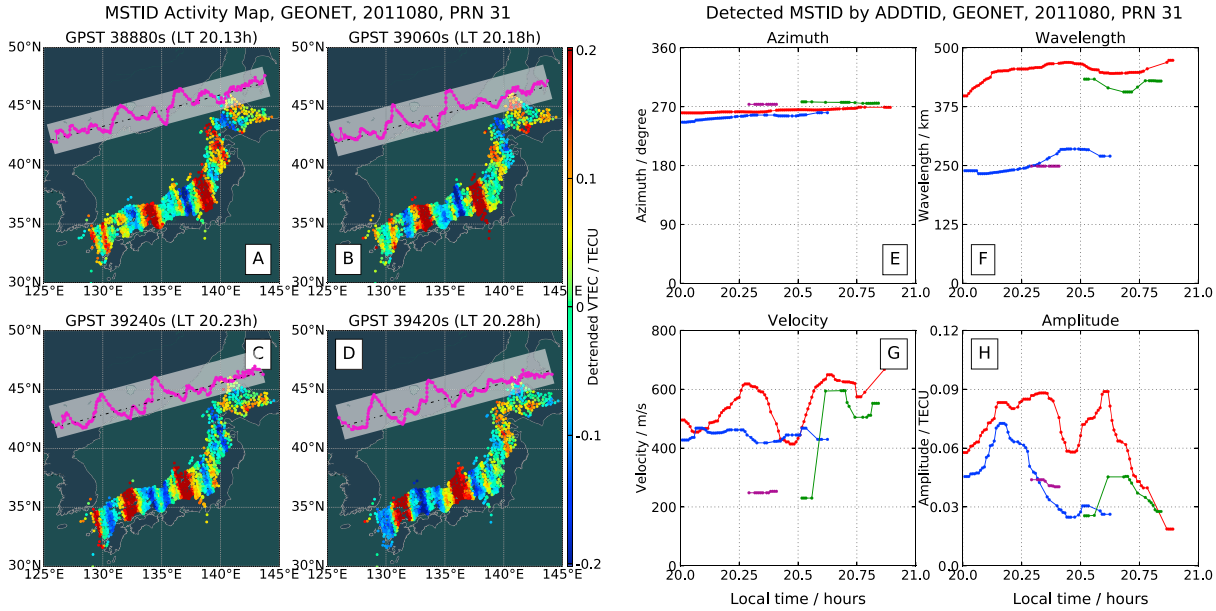

Figure 9. Two MSTIDs with different wavelengths that propagate in almost identical azimuths at nighttime, from GEONET, for satellite PRN 31, on the 80th day of 2011. (a–d) Two MSTID propagations of different wavelengths, as detrended VTEC maps along with the detrended VTEC projection onto the propagation azimuth coded in purple (in TECUs). At nighttime, 20:08–20:17 LT, for four snapshots at GPS time 38,880, 39,060, 39,240, and 39,420 s. (e–h) The corresponding time evolution of the two MSTIDs at nighttime (20:00–21:00 LT) by azimuth, wavelength, velocity, and amplitude.

superposition of two sinusoids of different amplitudes (one is up to 0.06 TECU, and the other is up to 0.09 TECU). Note also that the amplitude plot indicates that the MSTID associated with the longer wavelength was the dominant MSTID, which is compatible with the projected waveform and visually corresponds to the sum of a large-amplitude, long-wavelength sinusoid with that of a lower amplitude, shorter-wavelength sinusoid. Note that these two MSTIDs were found from the examination of the time series given by the ADDTID method (i.e., see Figures 9e–9h). The detection of this type of phenomena can be automated using simple rules on the temporal evolution of the parameters.

6.2.3. Different MSTIDs That Propagate in Almost Opposite Azimuths

Figure 10 shows the event where two MSTIDs propagate in opposite azimuths and are characterized by distinct parameters. The two wavefronts moving oppositely appear just before the morning solar terminator (about 5:00 LT) and can be clearly observed from the detrended VTEC maps (Figures 10a–10d).

Discussion. These two MSTIDs with similar amplitudes about 0.005 TECU are observed before the morning solar terminator (4:30–5:30 LT). The first MSTID propagates in the northeast direction and is located at the northeast corner of the map. This MSTID can be distinguished because it consists of a narrow wavefront occurring with a wavelength of about 140 km. The second MSTID can be distinguished because it consists of a flat and wide wavefront that propagates in the west/equator-west direction. This MSTID is in the southwest corner of the map, with wavelengths of about 200 km. These two MSTIDs were found from the examination of the time series given by the ADDTID method in Figures 10e–10h, by searching for MSTIDs with azimuth paths separated by 180°, and afterward confirming the findings on the VTEC maps.

6.2.4. Circular Waves in a Day Without Special Ionospheric Events

Next, we present the detection of circular waves in a day without special ionospheric events (see explanation at the beginning of section 6.2). In Figure 11, we show the correspondence between the visual appearance of the VTEC maps (Figures 11a–11d) and the temporal sequence of the estimated parameters (Figures 11e–11h).

Discussion. Although the algorithm is designed to detect plane waves, by looking at the time evolution of the parameters, we observe that the algorithm detects several MSTIDs that have azimuths compatible with the local plane approximations of the waveform of the circular waves observed in Figures 11a–11d. Previously, circular waves of the ionospheric disturbances have been reported [see, e.g., *Tsugawa et al.*, 2011], where the circular waves appear locally in the form of planar waves for each set of IPPs of a given GPS satellite. This is consistent with our findings. A manual estimation by means of a ruler on the left maps give results that are

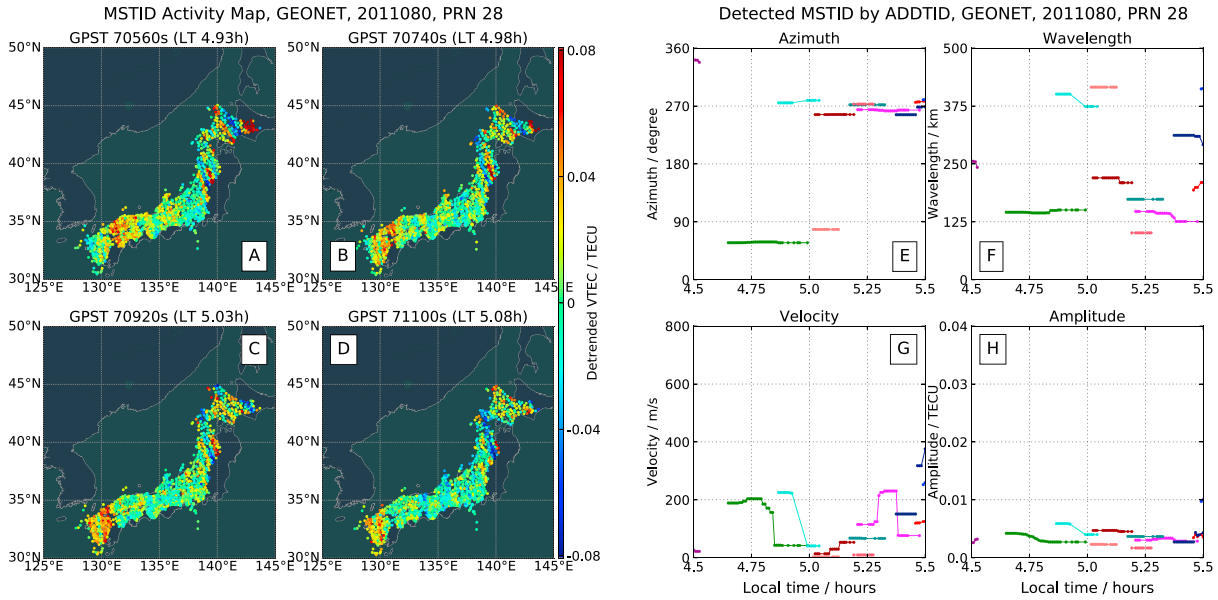

Figure 10. Two MSTIDs that propagate in almost opposite directions during the morning solar terminator at about 5:00 LT, from GEONET, for satellite PRN 28, on the 80th day of 2011. (a–d) The propagation pattern of two MSTIDs with opposite azimuth as detrended VTEC maps (in TECUs) at nighttime (4:56–5:05 LT), for four snapshots at GPS time 70,560, 70,740, 70,920, and 71,100 s. (e–h) The corresponding time evolution of the parameters at nighttime (4:30–5:30 LT) by azimuth, wavelength, velocity, and amplitude. Note that at 4:56–5:05 LT there are two MSTIDs with an azimuth difference of 180°.

almost equal to the parameters shown in Figures 11e–11h. This estimation is done from the local slope of the waves at different regions of the map, at a given time, for instance, at 17:30 LT. These local approximations to planar waves propagate in the northwest direction, with common values of the other parameters, such as wavelength about 100–200 km, velocity about 120–200 m/s, and the period about 1000 s. Note also the low variability of the wavelengths and velocities associated with each MSTID. In addition, the amplitude of the planar waves alternates, which hints at the fact that they all have almost the same energy. Note that the differences in the values of the wavelength and velocity arise because of the different widths of Japan. The difference in the precision is because in the center, more cycles are measured, while at the north or south

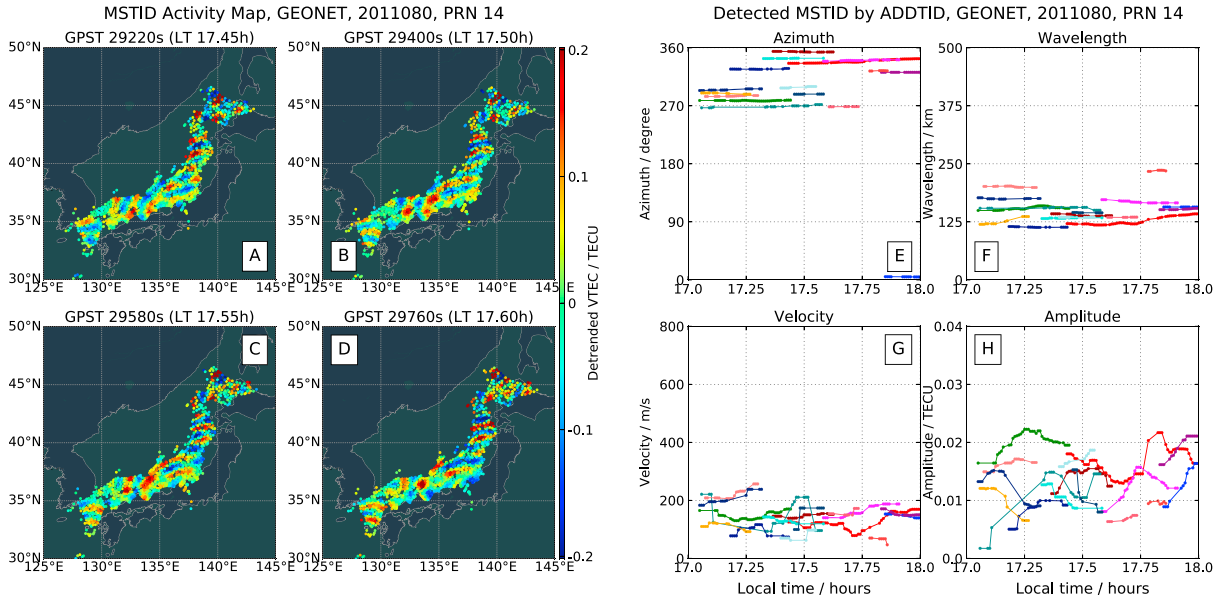

Figure 11. Circular-like MSTIDs during the evening solar terminator about 17:30 LT, from the GEONET, for satellite PRN 14, on the 80th day of 2011. (a–d) Circular MSTID in the detrended VTEC maps (in TECUs) at evening time (17:27–17:36 LT), for four snapshots at GPS time 29,220, 29,400, 29,580, and 29,760 s. (e–h) The time evolution of the estimated parameters during the time interval 17:00–18:00 LT, by azimuth, wavelength, velocity, and amplitude.

there is a lower number of cycles. Note that an automatic detection of the candidates for circular waves can be done from the temporal evolution of the parameters by means of simple rules.

This finding, obtained thanks to the extreme sensitivity of the new ADDTID technique, might be generated by two earthquakes of magnitude *M* 4.6 and *M* 4.9 in a 3 min interval (recorded at respectively 17:29 and 17:26 LT in *U.S. Geological Surve (USGS)* [2011a, 2011b]). These earthquakes occurred a few hundred seconds before the detected waves and are compatible with the center of the circular ionospheric wave. A similar precedent of a delay between occurrence of the 2011 Japan Tohoku earthquake and the circular wave disturbances detected over Japan is reported in *Tsugawa et al.* [2011]. In this case the delay was of about 7 min after the earthquake. The novelty of this finding, regarding previous works performed on major earthquakes (with magnitudes greater than 6), is the detection by the perturbation on the ionosphere despite the relative low magnitude of the earthquake.

7. Conclusion

We have presented the Atomic Decomposition Detector of MSTIDs (ADDTID), a comprehensive multi-MSTID detection technique, and successfully applied it in both simulated and actual data in wide and dense networks of GNSS permanent receivers, such as GEONET in Japan. The method that we have presented improves the previous cGII method [see *Hernández-Pajares et al.*, 2012] in the sense that it simultaneously can detect different MSTID planar waves and estimate their parameters. The new method is compared with the cGII method as a benchmark. The general properties are consistent with results of previous studies [e.g., *Jacobson et al.*, 1995; *Hernández-Pajares et al.*, 2006; *Tsugawa et al.*, 2007a, 2007b; *Hernández-Pajares et al.*, 2012; *Otsuka et al.*, 2013]. The main contribution of the method for the study of MSTIDs can be summarized as follows: (a) the distribution and tracking of simultaneous MSTID, i.e., temporal variation of the azimuth, velocity, amplitude, and wavelength, and the determination of the number of MSTIDs present at a given moment; (b) the observation of MSTIDs with velocities much higher than 400–600 m/s during nighttime and the solar terminator; (c) the detection of different simultaneous MSTIDs with the same azimuth or differences of azimuth of 180°; (d) the detection of circular waves that are compatible (in time and space) with the occurrence of two consecutive earthquakes of low magnitude; and (e) the possibility of creating rules for automatically finding special distributions of the MSTIDs without a visual inspection of the VTEC maps.

In the future, we will explore extensions of the wave model to include MSTID circular or elliptic waves, which appear in the case of earthquakes and are of interest and complement the study that we have presented. Note also that in some cases the planar wave model detects multiple, distinct MSTIDs with azimuthal patterns consistent with a spherical wave. This further justifies future work to incorporate circular or ecliptic wave models.

Appendix A: Implementation Details

A1. Two-Step Estimation of the MSTIDs Parameters

The MSTID model presented in equation (7) is characterized by three parameters: $\{\lambda, \theta, \varphi\}$. As the reconstruction error depends on the parameters through trigonometric functions, and a division, this error is more sensitive to some parameters than others. Specifically, the impact of small deviations of the parameters $\{\lambda, \theta\}$ on the final performance is much higher than the case of φ. The method is extremely precise in the estimation of the angle of propagation and wavelength, but the velocity estimation is less accurate, possibly because it is computed from differences of φ at each snapshot. Taking this into consideration, the estimation strategy will have two steps; in the first step, the parameters $\{\lambda, \theta\}$ are estimated using a dictionary fine grained in the range of these parameters and rough in $\{\varphi\}$. In the second step, the estimation is done with λ and θ fixed to the values of the first step, and the parameter φ will be used to construct a new dictionary with a fine-grained range of values.

The effect of splitting the estimation into two steps also has an important impact on the computational requirements of the problem. If the granularity (i.e., increments) on the values of each parameter were of *n*, the size of the dictionary would be $O(n^3)$. By dividing the estimation into two phases, the dictionary of the structure in equation (A4) gives a requirement of $O(n^2)$ for the first phase. The resulting nonzero-weight elements of the dictionary of the detected MSTID in the first phase *M* (where $M << N$) reduces the total number of operations on the second phase to $O(Mn)$. The range of values *n* needs to be adapted to the problem at hand, which depends on the margin of phases, frequencies, and azimuths of the MSTIDs that we want to detect.

Step I. Estimation of λ, θ, and the number of MSTIDs. For the estimation of $\{\lambda, \theta\}$, we can simplify the dictionary by means of simple trigonometry; the parameter φ of the elements $T_i(x, y)$ of the dictionary (see equation (7)) is absorbed by the amplitude of the wave. Thus, the element $T_i(x, y)$ for the snapshot t is

$$\alpha_i T_i(x,y) = \beta_i \cos\left(\frac{2\pi}{\lambda_i}\left(x\cdot\cos\theta_i + y\cdot\sin\theta_i\right)\right) + \gamma_i \sin\left(\frac{2\pi}{\lambda_i}\left(x\cdot\cos\theta_i + y\cdot\sin\theta_i\right)\right) \tag{A1}$$

which can be rearranged as two new dictionary elements as

$$T_{\beta i}(x,y) = \cos\left(\frac{2\pi}{\lambda_i}\left(x\cos\theta_i + y\sin\theta_i\right)\right) \tag{A2}$$

$$T_{\gamma i}(x,y) = \sin\left(\frac{2\pi}{\lambda_i}\left(x\cos\theta_i + y\sin\theta_i\right)\right) \tag{A3}$$

where β_i and γ_i are the amplitudes of the pair orthogonal sinusoidal basis, which satisfy the relationship of $\beta_i = \alpha_{ti}\cos(\varphi_i)$ and $\gamma_i = -\alpha_{ti}\sin(\varphi_i)$. Note that the values of β_i and γ_i are used only for deciding the set of elements of the dictionary $T_i(x, y)$ to be used in the following step.

Although the phase φ_i can be obtained from β_i and γ_i, by their ratio and the use of the *atan* function, this method is extremely unreliable, which justifies postponing the estimation of φ_i for step II. The estimation of φ is done in step II keeping the fixed values λ and θ estimated in step I.

The dictionary D_I for step I has the following structure:

$$D_I = [D_\beta, D_\gamma] = [T_{\beta 1}, T_{\beta 2}, \ldots, T_{\beta N}, T_{\gamma 1}, T_{\gamma 2}, \ldots, T_{\gamma N}] \tag{A4}$$

where $T_{\beta i}$ and $T_{\gamma i}$ denote the elements of the dictionary defined in equations (A2) and (A3) with the corresponding parameters $\theta_{\beta i}$, $\lambda_{\beta i}$ and $\theta_{\gamma i}$, $\lambda_{\gamma i}$. We denote the vectors of the weights associated with each estimated parameter as β_t and γ_t. Note that we did not introduce a constraint in the elements of the vectors β_t and γ_t so that they should be non-null simultaneously; we decided to take as candidates of MSTID the union of indices i found in both vectors, to filter the values in step II. That is, some of the candidates to be detected MSTIDs will be discarded in the second step. The map $V(x, y)$ at epoch t can be expressed as follows:

$$V(x,y) = D_I \cdot [\hat{\beta}_t, \hat{\gamma}_t]^T = D_\beta \cdot \hat{\beta}_t + D_\gamma \cdot \hat{\gamma}_t \tag{A5}$$

where the vector of coefficients $\hat{\beta}_t$ and $\hat{\gamma}_t$ are estimated by means of the LASSO algorithm. The elements of the dictionary D_I associated with the coefficients $\hat{\beta}_t$ and $\hat{\gamma}_t$ different from zero determine the wavelengths $\hat{\lambda}_t$ and directions $\hat{\theta}_t$ of each MSTID candidate and are the input for the next step.

Step II. Estimation of φ. In step I at epoch t, we detect a set of M possible MSTIDs candidates. We define the parameters of the ith detected MSTID at epoch t as the pair $(\hat{\lambda}_i, \hat{\theta}_i)$, which remains fixed in step II, where we create a new smaller dictionary for estimating the φ_i associated with each pair $(\hat{\lambda}_i, \hat{\theta}_i)$, from a new variable that is more suitable. We will denote it as B and is defined as $B_{(\hat{\lambda}_i\hat{\theta}_i)j} = \frac{\hat{\lambda}_i}{2\pi}\varphi_{(\hat{\lambda}_i\hat{\theta}_i)j}$ (see equations (A6) and (A7) below). Thus, given a pair $(\hat{\lambda}_i, \hat{\theta}_i)$, we create $j = 1, 2, \ldots, N$ possible values of $B_{(\hat{\lambda}_i\hat{\theta}_i)j}$. An error analysis showed that the expression (A7) has a lower sensitivity to the estimation error of φ_j than (A6). Hence, the dictionary is parametrized by $B_{(\hat{\lambda}_i\hat{\theta}_i)j}$.

The structure for the elements j associated with the pair $(\hat{\lambda}_i, \hat{\theta}_i)$ of the dictionary of step II will be as follows:

$$T_{(\hat{\lambda}_i\hat{\theta}_i)j}(x,y) = \cos\left(\frac{2\pi}{\hat{\lambda}_i}\left(x\cdot\cos\hat{\theta}_i + y\cdot\sin\hat{\theta}_i\right) + \varphi_{(\hat{\lambda}_i\hat{\theta}_i)j}\right) \tag{A6}$$

$$= \cos\left(\frac{2\pi}{\hat{\lambda}_i}\left(x\cdot\cos\hat{\theta}_i + y\cdot\sin\hat{\theta}_i + B_{(\hat{\lambda}_i\hat{\theta}_i)j}\right)\right) \tag{A7}$$

with $i = 1, 2, \ldots, M, j = 1, 2, \ldots, N$. Each element of the new dictionary will correspond to a given φ, and the structure of the new dictionary, which we will denote as D_{II}, is created by concatenation of the dictionaries

specific for each MSTID associated with each pair $(\hat{\lambda}_i, \hat{\theta}_i)$ detected in step I. Therefore, the dictionary associated with a given MSTID $D_{\hat{\lambda}_i\hat{\theta}_i}$ will consist of a set of waveforms that characterize the MSTID estimated for fixed values of $\hat{\theta}_i$ and $\hat{\lambda}_i$ and the range of values $B_{(\hat{\lambda}_i\hat{\theta}_i)j}$ related to the phase φ_j of the waveform.

$$D_{II} = \left[D_{\hat{\lambda}_1\hat{\theta}_1}, D_{\hat{\lambda}_2\hat{\theta}_2}, \ldots, D_{\hat{\lambda}_M\hat{\theta}_M}\right] = \left[T_{\hat{\lambda}_1\hat{\theta}_1 1}, T_{\hat{\lambda}_1\hat{\theta}_1 2}, \ldots, T_{\hat{\lambda}_M\hat{\theta}_M N}\right] \tag{A8}$$

Thus, if the range of possible values of $B_{(\hat{\lambda}_i\hat{\theta}_i)j}$ is N, the size of the dictionary D_{II} is $M \times N$ (M is the number of candidate MSTIDs from step I).

Note that dividing the estimation into two steps, in addition to solving the estimation uncertainty in φ_j, reduces the computational needs. That is, the combined size of the two dictionaries is $2N^2 + MN$, which is much smaller than the size N^3 needed for simultaneously computing all the parameters. For instance, if the resolution of θ, λ, and B are 2°, 2 km, and 0.1 km, respectively, assuming $M \leq 10$ in each snapshot, the size of the dictionary is $N^3 \approx 10^8$ versus $2N^2 + MN \approx 10^6$. The value of N was variable and depended on the resolution of each variable. Typically, the value of N was around 500.

A2. Dealing With Noise and Distortion

The difficulty of estimating the number of MSTIDs and their characteristics from an incomplete and nonuniform sampling is aggravated by the presence of noise that depends on the elevation of each satellite and of distortions due to the geometry. The noise and distortion can be summarized into two categories, which are dealt with differently by the algorithm ADDTID presented in this work.

Additive noise. The term $\frac{1}{2}\|V - D\alpha_t\|_{\ell_2} < \tau$ in the optimization problem allows for small deviations of the order of τ. Note that as the metric is quadratic, the underlying hypothesis is that this additive noise follows a Gaussian distribution.

Distortion due to multiplicative effects. These are effects that modify subsets of samples and can be understood as the inaccuracy in the estimation of the slant factor cos $\chi(t)$, loss of data from one station, cycle slips, elevation of the satellites, etc. These effects can be dealt with by extending the dictionary by means of a diagonal matrix of the size of the number of samples, that is, adding a diagonal subdictionary. This idea was introduced by *Wright et al.* [2009], to model the effect of occlusions in the context of image processing, and is appropriate for modeling the categories of distortion mentioned above. This diagonal subdictionary allows for assigning a specific value to the sampling points that have suffered an extreme degradation while allowing the set of global dictionary entries that model the MSTID as plane waves. The structure of the extended dictionary is as follows:

$$D_{M\times(N+M)} = [T_1, T_2, T_3, \ldots T_N, I_{M\times M}] \tag{A9}$$

Therefore, now the reconstruction of the plane wave model is given by

$$V(x,y) = \sum_{i=0}^{N} \alpha_i \cdot T_i(x,y) + \sum_{j=0}^{M} \delta_j \cdot I_j(x,y) \tag{A10}$$

where the diagonal term $I_{M\times M}$ in the dictionary allows for modeling effects on the isolated observations by means of the coefficient δ_j. Note that this coefficient is a dummy variable in the sense that it enters the optimization problem as a variable but is not used. The variables of interest are α_i, i.e., the coefficients of the elements of the dictionary related to the waves that we want to detect.

A3. Improvement: Reweighted LASSO

As mentioned in section 5.3, the LASSO algorithm allows for the reconstruction of the initial observation vector of pierce points by means of a sparse set of elements of a dictionary. This can be thought of as an approximation of ℓ_0 by means of ℓ_1. Nevertheless, the ℓ_1 solution still allowed for similar elements of the dictionary to have weights different from zero. The underlying physical phenomenon consists of a small number of significant MSTIDs with different velocities, azimuths, and wavelengths. To improve the sparseness of the solution, we have implemented a variant that provides a higher degree of sparsity than the original LASSO. This solution is based on iteratively solving the problem stated in equation (11) by reweighting the vector of estimated coefficients α from each intermediate solution. The idea proposed by *Candes et al.* [2008]

uses a diagonal weight matrix W designed to penalize the use of correlated elements of the dictionary in the reconstruction of the observation. The estimation of $\hat{\alpha}^{(j)}$ at the reweighting iteration j can be stated as

$$\hat{\alpha}^{(j)} = \arg\min_{\alpha} \frac{1}{2}\|V - D\alpha\|_2^2 + \rho\|W\alpha\|_1 \tag{A11}$$

where the diagonal of W consists of positive weights w_i ($i = 1, 2, \ldots, dim(\alpha)$), which redefines the influence of the MSTID wave atoms. The elements of the diagonal matrix W are defined as $w_i = \frac{1}{|\alpha_i| + \varepsilon_w}$, if $\alpha_i \neq 0$, otherwise $w_i = \infty$. The term $\varepsilon_w > 0$, which typically is slightly smaller than the mean of the elements of $\hat{\alpha}^{(j)}$, ensures that there are no divisions by zero. This normalization forces the solution $\hat{\alpha}^{(j)}$ to concentrate on the indices where w_i is small to prevent a penalization of larger coefficients in the regularization term.

Observe that the weighting term W in equation (A11) affects the regularization term, not the reconstruction error term. This rescaling method seeks to achieve the selection of the weights independent of the magnitude of the approximation coefficients $\hat{\alpha}$. An interesting property of this method is that the convergence is fast. We have found empirically (also mentioned in *Candes et al.* [2008]) that only two or three iterations are needed for convergence. Although the method introduces a normalization of the α, the relative amplitude of the MSTIDs is preserved.

Acknowledgments
This work was supported by the project TEC2015-69266-P (MINECO/FEDER, UE). We also acknowledge the scholarship from China Scholarship Council (CSC) under the grant CSC 201508390017. We acknowledge that the GPS data of GEONET are provided by the Geospatial Information Authority of Japan (GSI). We would like to thank Nathaniel Frissell, for the helpful comments that have improved the manuscript. Also, we would like to thank the anonymous reviewers for their comments that have also improved the first version of the manuscript. All the code of this project was done in Python using the machine learning library scikit-learn. The data for this paper are available, and they can be requested from any of the authors in particular from Heng Yang (h.yang@upc.edu) and Enrique Monte-Moreno (enric.monte@upc.edu).

References

Afraimovich, E., I. Edemskiy, A. Leonovich, L. Leonovich, S. Voeykov, and Y. V. Yasyukevich (2009), MHD nature of night-time MSTIDs excited by the solar terminator, *Geophys. Res. Lett.*, *36*, L15106, doi:10.1029/2009GL039803.

Bilitza, D., D. Altadill, Y. Zhang, C. Mertens, V. Truhlik, P. Richards, L.-A. McKinnell, and B. Reinisch (2014), The International Reference Ionosphere 2012—A model of international collaboration, *J. Space Weather Space Clim.*, *4*, A07.

Candes, E. J., M. B. Wakin, and S. P. Boyd (2008), Enhancing sparsity by reweighted $\ell 1$ minimization, *J. Fourier Anal. Appl.*, *14*(5–6), 877–905.

Chen, C., A. Saito, C. Lin, M. Yamamoto, S. Suzuki, and G. Seemala (2016), Medium-scale traveling ionospheric disturbances by three-dimensional ionospheric GPS tomography, *Earth Planets Space*, *68*(1), 1–9.

Chen, S. S., D. L. Donoho, and M. A. Saunders (2001), Atomic decomposition by basis pursuit, *SIAM Rev.*, *43*(1), 129–159.

Chilcote, M., J. LaBelle, F. Lind, A. Coster, E. Miller, I. Galkin, and A. Weatherwax (2015), Detection of traveling ionospheric disturbances by medium-frequency Doppler sounding using AM radio transmissions, *Radio Sci.*, *50*, 249–263, doi:10.1002/2014RS005617.

Deng, Z., S. Schön, H. Zhang, M. Bender, and J. Wickert (2013), Medium-scale traveling ionospheric disturbances (MSTID) modeling using a dense German GPS network, *Adv. Space Res.*, *51*(6), 1001–1007.

Ding, F., W. Wan, G. Xu, T. Yu, G. Yang, and J.-S. Wang (2011), Climatology of medium-scale traveling ionospheric disturbances observed by a GPS network in central China, *J. Geophys. Res.*, *116*, A09327, doi:10.1029/2011JA016545.

Dow, J. M., R. Neilan, and C. Rizos (2009), The International GNSS Service in a changing landscape of Global Navigation Satellite Systems, *J. Geod.*, *83*(3–4), 191–198.

Fischler, M. A., and R. C. Bolles (1981), Random Sample Consensus: A paradigm for model fitting with applications to image analysis and automated cartography, *Commun. ACM*, *24*(6), 381–395.

Hastie, T., R. Tibshirani, and J. Friedman (2009), *The Elements of Statistical Learning: Data Mining, Inference, and Prediction*, 2nd ed., Springer Series in Statistics, New York.

Hastie, T., R. Tibshirani, and M. Wainwright (2015), *Statistical Learning With Sparsity: The Lasso and Generalizations*, CRC Press, Boca Raton, Fla.

Hernández-Pajares, M., J. Juan, J. Sanz, and O. Colombo (2002), Improving the real-time ionospheric determination from GPS sites at very long distances over the equator, *J. Geophys. Res.*, *107*, 1296, doi:10.1029/2001JA009203.

Hernández-Pajares, M., J. Juan, and J. Sanz (2006), Medium-scale traveling ionospheric disturbances affecting GPS measurements: Spatial and temporal analysis, *J. Geophys. Res.*, *111*, A07S11, doi:10.1029/2005JA011474.

Hernández-Pajares, M., J. Juan, J. Sanz, R. Orus, A. Garcia-Rigo, J. Feltens, A. Komjathy, S. Schaer, and A. Krankowski (2009), The IGS VTEC maps: A reliable source of ionospheric information since 1998, *J. Geod.*, *83*(3–4), 263–275.

Hernández-Pajares, M., J. M. Juan, J. Sanz, À. Aragón-Àngel, A. García-Rigo, D. Salazar, and M. Escudero (2011), The ionosphere: Effects, GPS modeling and the benefits for space geodetic techniques, *J. Geod.*, *85*(12), 887–907.

Hernández-Pajares, M., J. Juan, J. Sanz, and A. Aragón-Àngel (2012), Propagation of medium scale traveling ionospheric disturbances at different latitudes and solar cycle conditions, *Radio Sci.*, *47*(6), RS0K05, doi:10.1029/2011RS004951.

Hernández-Pajares, M., et al. (2017), Direct MSTID mitigation in precise GPS processing, *Radio Sci.*, *52*, 321–337, doi:10.1002/2016RS006159.

Hocke, K., and K. Schlegel (1996), A review of atmospheric gravity waves and travelling ionospheric disturbances: 1982–1995, *Ann. Geophys.*, *14*(9), 917–940.

Huang, F., X. Dou, J. Lei, J. Lin, F. Ding, and J. Zhong (2016), Statistical analysis of nighttime medium-scale traveling ionospheric disturbances using airglow images and GPS observations over central China, *J. Geophys. Res. Space Physics*, *121*, 8887–8899, doi:10.1002/2016JA022760.

Hunsucker, R. D. (1982), Atmospheric gravity waves generated in the high-latitude ionosphere: A review, *Rev. Geophys.*, *20*(2), 293–315.

Jacobson, A. R., R. C. Carlos, R. S. Massey, and G. Wu (1995), Observations of traveling ionospheric disturbances with a satellite-beacon radio interferometer: Seasonal and local time behavior, *J. Geophys. Res.*, *100*(A2), 1653–1665.

Kelley, M. C. (2011), On the origin of mesoscale TIDs at midlatitudes, *Ann. Geophys.*, *29*(2), 361–366.

Kotake, N., Y. Otsuka, T. Ogawa, T. Tsugawa, and A. Saito (2007), Statistical study of medium-scale traveling ionospheric disturbances observed with the GPS networks in Southern California, *Earth Planets Space*, *59*(2), 95–102.

Lee, J. K., F. Kamalabadi, and J. J. Makela (2008), Three-dimensional tomography of ionospheric variability using a dense GPS receiver array, *Radio Sci.*, *43*(3), RS3001, doi:10.1029/2007RS003716.

Mevius, M., et al. (2016), Probing ionospheric structures using the LOFAR radio telescope, *Radio Sci.*, *51*, 927–941, doi:10.1002/2016RS006028.

National Aeronautics and Space Administration/Goddard Space Flight Center (NASA/GSFC) (2012), International Reference Ionosphere 2012 (IRI-2012) Database. [Available at https://omniweb.gsfc.nasa.gov/vitmo/iri2012_vitmo.html, accessed 1–May–2017.]

Ogawa, T., N. Nishitani, Y. Otsuka, K. Shiokawa, T. Tsugawa, and K. Hosokawa (2009), Medium-scale traveling ionospheric disturbances observed with the SuperDARN Hokkaido radar, all-sky imager, and GPS network and their relation to concurrent sporadic E irregularities, *J. Geophys. Res.*, *114*, A03316, doi:10.1029/2008JA013893.

Oinats, A. V., V. I. Kurkin, and N. Nishitani (2015), Statistical study of medium-scale traveling ionospheric disturbances using SuperDARN Hokkaido ground backscatter data for 2011, *Earth Planets Space*, *67*(1), 1–9.

Otsuka, Y., K. Shiokawa, T. Ogawa, and P. Wilkinson (2004), Geomagnetic conjugate observations of medium-scale traveling ionospheric disturbances at midlatitude using all-sky airglow imagers, *Geophys. Res. Lett.*, *31*, L15803, doi:10.1029/2004GL020262.

Otsuka, Y., N. Kotake, K. Shiokawa, T. Ogawa, T. Tsugawa, and A. Saito (2011), Statistical study of medium-scale traveling ionospheric disturbances observed with a GPS receiver network in Japan, in *Aeronomy of the Earth's Atmosphere and Ionosphere*, vol. 2, pp. 291–299, Springer, Dordrecht, Netherlands.

Otsuka, Y., K. Suzuki, S. Nakagawa, M. Nishioka, K. Shiokawa, and T. Tsugawa (2013), GPS observations of medium-scale traveling ionospheric disturbances over Europe, *Ann. Geophys.*, *31*(2), 163–172.

Sagiya, T. (2004), A decade of GEONET: 1994–2003, *Earth Planets Space*, *56*(8), xxix–xli.

Saito, A., S. Fukao, and S. Miyazaki (1998), High resolution mapping of TEC perturbations with the GSI GPS network over Japan, *Geophys. Res. Lett.*, *25*(16), 3079–3082.

Shiokawa, K., C. Ihara, Y. Otsuka, and T. Ogawa (2003), Statistical study of nighttime medium-scale traveling ionospheric disturbances using midlatitude airglow images, *J. Geophys. Res.*, *108*, 1052, doi:10.1029/2002JA009491.

Ssessanga, N., Y. H. Kim, and E. Kim (2015), Vertical structure of medium-scale traveling ionospheric disturbances, *Geophys. Res. Lett.*, *42*, 9156–9165, doi:10.1002/2015GL066093.

Stefanello, M., M. Muella, D. Amorim, C. Machado, J. Bageston, A. Pimenta, C. Martinis, C. Sullivan, J. Bittencourt, and N. Schuch (2015), OI 630.0 nm all-sky image observations of medium-scale traveling ionospheric disturbances at geomagnetic conjugate points, *J. Atmos. Sol. Terr. Phys.*, *128*, 58–69.

Tibshirani, R. (1996), Regression shrinkage and selection via the Lasso, *J. R. Stat. Soc. Ser. B*, *58*, 267–288.

Tsugawa, T., K. Shiokawa, Y. Otsuka, T. Ogawa, A. Saito, and M. Nishioka (2006), Geomagnetic conjugate observations of large-scale traveling ionospheric disturbances using GPS networks in Japan and Australia, *J. Geophys. Res.*, *111*, A02302, doi:10.1029/2005JA011300.

Tsugawa, T., N. Kotake, Y. Otsuka, and A. Saito (2007a), Medium-scale traveling ionospheric disturbances observed by GPS receiver network in Japan: A short review, *GPS Solutions*, *11*(2), 139–144.

Tsugawa, T., Y. Otsuka, A. Coster, and A. Saito (2007b), Medium-scale traveling ionospheric disturbances detected with dense and wide TEC maps over North America, *Geophys. Res. Lett.*, *34*, L22101, doi:10.1029/2007GL031663.

Tsugawa, T., A. Saito, Y. Otsuka, M. Nishioka, T. Maruyama, H. Kato, T. Nagatsuma, and K. Murata (2011), Ionospheric disturbances detected by GPS total electron content observation after the 2011 off the Pacific coast of Tohoku earthquake, *Earth Planets Space*, *63*(7), 875–879.

U.S. Department of Commerce, N. O. a. A. A. (2011a), Earthquake Data and Information. [Available at https://www.ngdc.noaa.gov/hazard/earthqk.shtml, accessed 20–July–2016.]

U.S. Department of Commerce, N. O. a. A. A. (2011b), Tsunami Data and Information. [Available at https://www.ngdc.noaa.gov/hazard/tsu.shtml, accessed 20–July–2016.]

U.S. Department of Commerce, N. O. a. A. A. (2011c), Solar Data Services: Sun, Solar Activity and Upper Atmosphere Data. [Available at https://www.ngdc.noaa.gov/stp/solar/solardataservices.html, accessed 20–July–2016.]

U.S. Department of Commerce, N. O. a. A. A. (2011d), Geomagnetic Calculators, Maps, Models, and Software. [Available at http://www.ngdc.noaa.gov/geomag/models.shtml, accessed 20–July–2016.]

U.S. Geological Surve (USGS) (2011a), Earthquake Summary, Magnitude 4.6, Near Honshu Japan. [Available at https://earthquake.usgs.gov/earthquakes/eventpage/usp000hy51#executive Date: 2011–03–21 08:09:26 UTC; Location: 39.195° N, 142.625° E; Depth: 49.9 km.]

U.S. Geological Surve (USGS) (2011b), Earthquake Summary, Magnitude 4.9, Near Honshu Japan. [Available at https://earthquake.usgs.gov/earthquakes/eventpage/usp000hy50#executive Date: 2011–03–21 08:06:22 UTC; Location: 36.452°N, 141.537°E; Depth: 21.4 km.]

Wright, J., A. Y. Yang, A. Ganesh, S. S. Sastry, and Y. Ma (2009), Robust face recognition via sparse representation, *IEEE Trans. Pattern Anal. Mach. Intell.*, *31*(2), 210–227.